

# Modeling of the High Column Density systems in The Lyman-Alpha Forest

T. Tan<sup>1,2,3</sup>, J. Rich<sup>1,2</sup>, E. Chaussidon<sup>4</sup>, J.M. Le Goff<sup>1</sup>,  
 C. Balland<sup>2</sup>, E. Armengaud<sup>1</sup>, J. Aguilar<sup>4</sup>, S. Ahlen<sup>5</sup>,  
 D. Bianchi<sup>6,7</sup>, D. Brooks<sup>8</sup>, T. Claybaugh<sup>4</sup>, A. Cuceu<sup>4</sup>, A. de  
 la Macorra<sup>9</sup>, P. Doel<sup>8</sup>, J. E. Forero-Romero<sup>10,11</sup>,  
 E. Gaztañaga<sup>12,13,14</sup>, S. Gontcho A Gontcho<sup>4,15</sup>, G. Gutierrez<sup>16</sup>,  
 H. K. Herrera-Alcantar<sup>17,1</sup>, K. Honscheid<sup>18,19,20</sup>, M. Ishak<sup>21</sup>,  
 D. Kirkby<sup>22</sup>, T. Kisner<sup>4</sup>, A. Kremin<sup>4</sup>, M. Landriau<sup>4</sup>,  
 L. Le Guillou<sup>2</sup>, M. Manera<sup>23,24</sup>, P. Martini<sup>18,25,20</sup>,  
 R. Miquel<sup>26,24</sup>, S. Nadathur<sup>13</sup>, N. Palanque-Delabrouille<sup>1,4</sup>,  
 F. Prada<sup>27</sup>, I. Pérez-Ràfols<sup>28</sup>, G. Rossi<sup>29</sup>, E. Sanchez<sup>30</sup>,  
 D. Schlegel<sup>4</sup>, M. Schubnell<sup>31,32</sup>, H. Seo<sup>33</sup>, J. Silber<sup>4</sup>,  
 D. Sprayberry<sup>34</sup>, G. Tarlé<sup>32</sup>, M. Walther<sup>35,36</sup>, B. A. Weaver<sup>34</sup>,  
 H. Zou<sup>37</sup>

<sup>1</sup>IRFU, CEA, Université Paris-Saclay, F-91191 Gif-sur-Yvette, France

<sup>2</sup>Sorbonne Université, CNRS/IN2P3, Laboratoire de Physique Nucléaire et de Hautes Energies (LPNHE), FR-75005 Paris, France

<sup>3</sup>CNRS-UCB International Research Laboratory, Centre Pierre Binétruy, IRL2007, CPB-IN2P3, Berkeley, US

<sup>4</sup>Lawrence Berkeley National Laboratory, 1 Cyclotron Road, Berkeley, CA 94720, USA

<sup>5</sup>Department of Physics, Boston University, 590 Commonwealth Avenue, Boston, MA 02215 USA

<sup>6</sup>Dipartimento di Fisica “Aldo Pontremoli”, Università degli Studi di Milano, Via Celoria 16, I-20133 Milano, Italy

<sup>7</sup>INAF-Osservatorio Astronomico di Brera, Via Brera 28, 20122 Milano, Italy

<sup>8</sup>Department of Physics & Astronomy, University College London, Gower Street, London, WC1E 6BT, UK

<sup>9</sup>Instituto de Física, Universidad Nacional Autónoma de México, Circuito de la Investigación Científica, Ciudad Universitaria, Cd. de México C. P. 04510, México

<sup>10</sup>Departamento de Física, Universidad de los Andes, Cra. 1 No. 18A-10, Edificio Ip, CP 111711, Bogotá, Colombia

- <sup>11</sup>Observatorio Astronómico, Universidad de los Andes, Cra. 1 No. 18A-10, Edificio H, CP 111711 Bogotá, Colombia
- <sup>12</sup>Institut d'Estudis Espacials de Catalunya (IEEC), c/ Esteve Terradas 1, Edifici RDIT, Campus PMT-UPC, 08860 Castelldefels, Spain
- <sup>13</sup>Institute of Cosmology and Gravitation, University of Portsmouth, Dennis Sciama Building, Portsmouth, PO1 3FX, UK
- <sup>14</sup>Institute of Space Sciences, ICE-CSIC, Campus UAB, Carrer de Can Magrans s/n, 08913 Bellaterra, Barcelona, Spain
- <sup>15</sup>University of Virginia, Department of Astronomy, Charlottesville, VA 22904, USA
- <sup>16</sup>Fermi National Accelerator Laboratory, PO Box 500, Batavia, IL 60510, USA
- <sup>17</sup>Institut d'Astrophysique de Paris. 98 bis boulevard Arago. 75014 Paris, France
- <sup>18</sup>Center for Cosmology and AstroParticle Physics, The Ohio State University, 191 West Woodruff Avenue, Columbus, OH 43210, USA
- <sup>19</sup>Department of Physics, The Ohio State University, 191 West Woodruff Avenue, Columbus, OH 43210, USA
- <sup>20</sup>The Ohio State University, Columbus, 43210 OH, USA
- <sup>21</sup>Department of Physics, The University of Texas at Dallas, 800 W. Campbell Rd., Richardson, TX 75080, USA
- <sup>22</sup>Department of Physics and Astronomy, University of California, Irvine, 92697, USA
- <sup>23</sup>Departament de Física, Serra Hünter, Universitat Autònoma de Barcelona, 08193 Bellaterra (Barcelona), Spain
- <sup>24</sup>Institut de Física d'Altes Energies (IFAE), The Barcelona Institute of Science and Technology, Edifici Cn, Campus UAB, 08193, Bellaterra (Barcelona), Spain
- <sup>25</sup>Department of Astronomy, The Ohio State University, 4055 McPherson Laboratory, 140 W 18th Avenue, Columbus, OH 43210, USA
- <sup>26</sup>Institució Catalana de Recerca i Estudis Avançats, Passeig de Lluís Companys, 23, 08010 Barcelona, Spain
- <sup>27</sup>Instituto de Astrofísica de Andalucía (CSIC), Glorieta de la Astronomía, s/n, E-18008 Granada, Spain
- <sup>28</sup>Departament de Física, EEBE, Universitat Politècnica de Catalunya, c/Eduard Maristany 10, 08930 Barcelona, Spain
- <sup>29</sup>Department of Physics and Astronomy, Sejong University, 209 Neungdong-ro, Gwangjin-gu, Seoul 05006, Republic of Korea
- <sup>30</sup>CIEMAT, Avenida Complutense 40, E-28040 Madrid, Spain
- <sup>31</sup>Department of Physics, University of Michigan, 450 Church Street, Ann Arbor, MI 48109, USA
- <sup>32</sup>University of Michigan, 500 S. State Street, Ann Arbor, MI 48109, USA
- <sup>33</sup>Department of Physics & Astronomy, Ohio University, 139 University Terrace, Athens, OH 45701, USA
- <sup>34</sup>NSF NOIRLab, 950 N. Cherry Ave., Tucson, AZ 85719, USA
- <sup>35</sup>Excellence Cluster ORIGINS, Boltzmannstrasse 2, D-85748 Garching, Germany
- <sup>36</sup>University Observatory, Faculty of Physics, Ludwig-Maximilians-Universität, Scheinerstr. 1, 81677 München, Germany
- <sup>37</sup>National Astronomical Observatories, Chinese Academy of Sciences, A20 Datun Road, Chaoyang District, Beijing, 100101, P. R. China

E-mail: [ting.tan@cea.fr](mailto:ting.tan@cea.fr), [james.rich@cea.fr](mailto:james.rich@cea.fr)

**Abstract.** The Lyman- $\alpha$  forests observed in the spectra of high-redshift quasars can be used as a tracer of the cosmological matter density to study baryon acoustic oscillations (BAO) and the Alcock-Paczynski effect. Extraction of cosmological information from these studies requires modeling of the forest correlations. While the models depend most importantly on the bias parameters of the intergalactic medium (IGM), they also depend on the numbers and characteristics of high-column-density systems (HCDs) ranging from Lyman-limit systems with column densities  $\log N_{\text{HI}}/\text{cm}^{-2} > 17$  to damped Lyman- $\alpha$  systems (DLAs) with  $\log N_{\text{HI}}/\text{cm}^{-2} > 20.2$ . These HCDs introduce broad damped absorption characteristic of a Voigt profile. Consequently they imprint a component on the power spectrum whose modes in the radial direction are suppressed, leading to a scale-dependent bias. Using mock data sets of known HCD content, we test a model that describes this effect in terms of the distribution of column densities of HCDs, the Fourier transforms of their Voigt profiles and the bias of the halos containing the HCDs. Our results show that this physically well-motivated model describes the effects of HCDs with an accuracy comparable to that of the ad-hoc models used in published forest analyses. We also discuss the problems of applying the model to real data, where the HCD content and their bias is uncertain.

---

## Contents

<b>1</b>	<b>Introduction</b>	<b>1</b>
<b>2</b>	<b>Analysis procedure of forest correlations</b>	<b>3</b>
<b>3</b>	<b>The model for correlations with HCDs</b>	<b>5</b>
<b>4</b>	<b>Tests with mocks</b>	<b>8</b>
4.1	Fits with the Voigt model	9
4.2	Comparison with the Exp model	10
<b>5</b>	<b>Fits with eBOSS data</b>	<b>14</b>
<b>6</b>	<b>Conclusion and Discussion</b>	<b>17</b>
<b>7</b>	<b>Data availability</b>	<b>17</b>
<b>A</b>	<b>Derivation of the Voigt and Exp models</b>	<b>17</b>
A.1	Absorption due to the Voigt profile	18
A.2	Linear bias of HCD absorption	19
A.3	Relation with the Exponential model	19
A.4	Redshift space distortions	20
A.5	Contaminated Kaiser model	20
A.6	Comparison to MW11	21
A.7	Comparison to FM12	21
A.8	Comparison to Rogers et al. (2018)	22
<b>B</b>	<b>Complete results of fits</b>	<b>22</b>

---

## 1 Introduction

Lyman- $\alpha$  forests, detected as a wavelength-dependent absorption in quasar spectra, can be used as biased tracers for the underlying dark matter density field. The forests have been used to measure the baryon acoustic oscillations (BAO) at a high redshift  $z > 2$  through the forest auto correlations [1–5], quasar-forest cross-correlations [6–8] and the combination of the two [9–11]. The Alcock-Paczynski effect has also been studied [12]. These studies have used the quasar spectra collected from the BOSS [13] and eBOSS programs [14, 15], and the on-going Dark Energy Spectroscopic Instrument (DESI) program [16–18] described in detail in [10, 11, 19–33].

Most forest absorption is due to neutral Hydrogen in the intergalactic medium (IGM) and its relation to the underlying matter fluctuations is understood through the fluctuating Gunn-Peterson approximation (FGPA) [34]. The amplitude of long-range correlations involving the diffuse IGM component of the forest can be modeled with the introduction of bias parameters giving the proportionality between forest and matter fluctuations. Additional absorption due to high-column density systems (HCDs) when the line of sight passes near a galaxy (the circumgalactic medium) or through a galaxy (the interstellar medium) is not caused by the

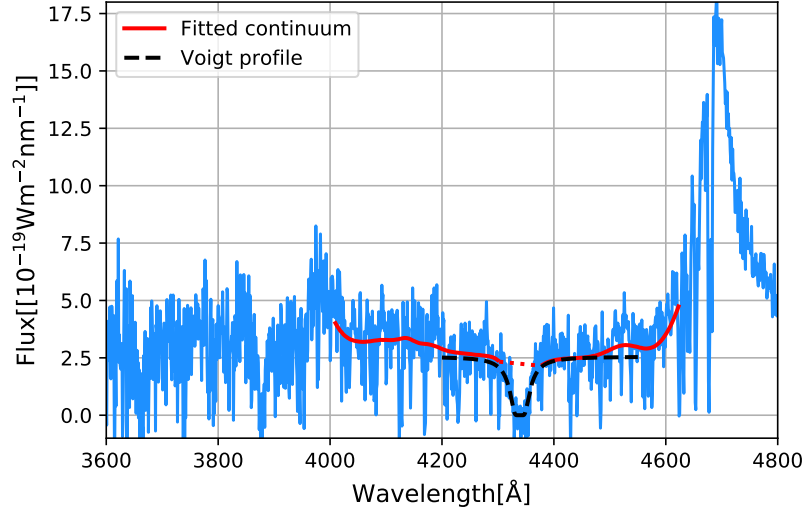


**Figure 1.** A flux spectrum,  $f_q(\lambda)$ , for a mock quasar, with  $z_{\text{QSO}} = 2.86$ . The Ly $\alpha$  emission line is present at 4685Å and a DLA with  $N_{\text{HI}} = 10^{20.72}\text{cm}^{-2}$  at redshift  $z_{\text{DLA}} = 2.57$  is present at 4339.9Å. The red line shows the estimated mean spectrum,  $\bar{F}(\lambda)C_q(\lambda)$ , about which the fluctuations are measured. The red dotted line indicates the region that is masked in the standard picca analysis. The black line shows the fitted Voigt profile fit to this DLA.

diffuse IGM. This complicates the forest correlations because their absorption profiles spread out the correlations radially. In the power spectrum, this suppresses modes of large  $k_{\parallel}$ , the component of  $k$  along the line of sight, leading to scale-dependent bias parameters. The purpose of this paper is to study the modeling of this effect for HCDs with column densities  $> 10^{17.2}\text{cm}^{-2}$ .

Figure 1 shows the spectrum of a quasar of redshift  $z_{\text{QSO}} = 2.86$  from mock data sets described in Etourneau et al. [35]. The fluctuating absorption on the blue side of Ly $\alpha$  emission ( $\lambda = 4685\text{Å}$ ) is mostly due to HI absorption in the IGM but there is an additional absorption at  $\lambda = 4340\text{Å}$  due to a HCD of column density  $N_{\text{HI}} = 10^{20.72}\text{cm}^{-2}$  at a redshift  $z_{\text{HCD}} = 2.57$ .

Such HCD's with  $N_{\text{HI}} > 10^{20.3}\text{cm}^{-2}$  are called damped Ly $\alpha$  systems (DLAs). DLAs are seen as strong absorption regions in quasar spectra, and can be modeled using the Voigt profile (Fig. 2), a convolution of the Lorentzian absorption profile and Gaussian thermal broadening. DLAs are detectable using Voigt profile fitting [36–38] or machine learning algorithms [39–43]. The bias of DLAs considered as discrete objects is measurable through the cross-correlation of DLAs with Ly $\alpha$  forests [44–46] or through cross-correlation with CMB lensing [47]. About 6% for Ly $\alpha$  forests of quasars with redshift  $\approx 2.5$  contain a DLA in the wavelength range between the Ly $\alpha$  and Ly $\beta$  emission lines [38, 42].

To minimize the complication of modeling the suppression of large- $k_{\parallel}$  modes in the forest power spectrum, detected DLAs can be masked from quasar spectra, as illustrated in Fig. 1. The masking is, however, imperfect, because DLAs in low signal-to-noise forests cannot be detected and masked. Furthermore, HCDs with  $N_{\text{HI}} < 10^{20.3}\text{cm}^{-2}$  cannot be detected and have a non-negligible effect on the Ly $\alpha$  correlation function. A model of this effect on large scales was developed in McQuinn and White [48] (noted MW11 hereafter) and Font-Ribera and Miralda-Escudé [49] (noted FM12 hereafter) and further developed in [50]. These models relate the damping of the radial correlations to the Fourier transform of the Voigt profiles

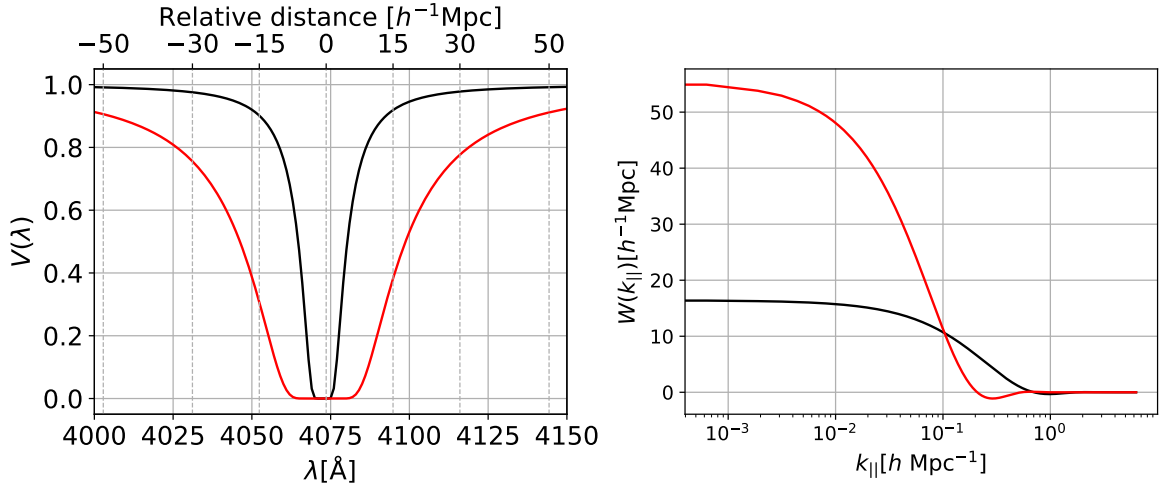


**Figure 2.** The Voigt transmission profile,  $V(\lambda)$  and the Fourier transform,  $W(k)$  of  $W(\lambda) = 1 - V(\lambda)$  for HCDs with  $N_{\text{HI}} = 10^{20} \text{ cm}^{-2}$  (black) and  $10^{21} \text{ cm}^{-2}$  (red) at a redshift of 2.35. The distance and  $k_{\parallel}$  scales are derived from the wavelength scale using the fiducial cosmological model.

of the HCDs and to the bias of the halos containing the HCDs. They have not yet been used in the published analyses of BOSS, eBOSS and DESI data, which have all modeled the power-spectrum cutoff at high  $k_{\parallel}$  with functional forms inspired by Ly $\alpha$  forest simulations [50, 51].

The purpose of this paper is to evaluate the accuracy of the models of MW11 and FM12 in describing the effects of HCDs on forest correlations in the case where the numbers and biases of the HCD's are known. To this end, we use the sets of mock quasar spectra described in Etourneau et al. [35]. These mock spectra were produced with realistic forest auto-correlations and quasar-forest cross-correlations, and with spectral resolution characteristic of the eBOSS and/or DESI programs. Most importantly, the mocks are produced with HCDs with the expected column-density distribution and with a bias consistent with that measured for DLAs.

This paper is organized as follows. In Section 2, we describe the procedure to measure the auto-correlations of Ly $\alpha$  absorption and its cross-correlations with quasars. In Section 3 we describe the theoretical framework of our model of forest correlations. In Section 4 we present tests of the models using mock data. Section 5 presents fits of the eBOSS data and discuss the problems that occur when the numbers of HCD's and their biases are not known. We conclude in Section 6.

## 2 Analysis procedure of forest correlations

In this section we list the steps needed to measure the Ly $\alpha$  forest flux transmission field and its auto-correlation and cross-correlation with discrete tracers like quasars. The implementation of these steps is done with the standard eBOSS and DESI pipeline package *picca*<sup>1</sup> [52]. The details of all steps are described for instance in [9].

The geometry of the correlation measurements are illustrated in Fig. 3. The main steps of the measurement are as follows:

<sup>1</sup><https://github.com/igmhub/picca>

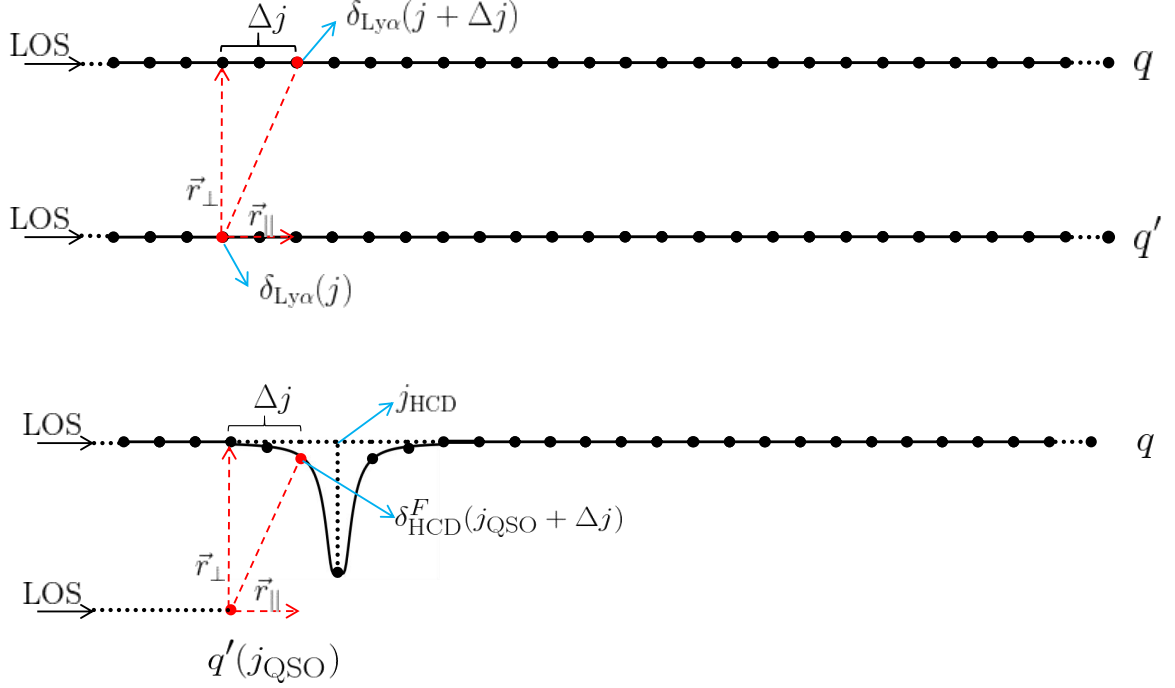


**Figure 3.** Illustration of the flux-flux auto-correlations and quasar-flux cross-correlations. The top two lines of sight illustrate flux-flux auto-correlation for two forests in front of quasars  $q$  and  $q'$ . The bottom two lines of sight illustrate the quasar-flux cross-correlation. Flux measurements  $f_q(\lambda)$  along the LOS to quasar  $q$  and the associated flux-transmission field  $\delta_q(\lambda)$  are measured on “pixels” of width  $\Delta \log \lambda = 0.0001$  (BOSS and eBOSS) or  $\Delta \lambda = 0.8 \text{ \AA}$  (DESI) as represented by the dots and indexed by  $j$ . On the bottom plot a HCD is centered on a wavelength indexed by  $j_{\text{HCD}}$ . Correlations of  $\delta_q(\lambda)$  with a neighboring pixel or quasar are measured as a function of  $(r_\perp, r_\parallel)$  calculated from the pixel wavelength separation and angular separation of the two lines-of-sight assuming a fiducial cosmological model.

1. Establishment of a catalog of quasars, their forests, and DLAs in the forests. For mocks data, the input list of quasars and their redshifts is known while for the data, the quasar catalog is constructed by algorithms used to determine the nature of the observed spectra (quasar, galaxy, star). The forests of each quasar are defined over the restframe wavelength range  $1040 < \lambda_{\text{RF}} < 1200 \text{ \AA}$ . We discard observed wavelengths  $< 3600 \text{ \AA}$  where the CCD throughput is very low. The DLAs in mock data are known while for the data DLA-finding algorithms must be used to construct a catalog and determine redshifts and column densities. The completeness and purity of the resulting DLA catalogs vary with the quasar signal to noise and the system column density. If a DLA masking strategy is adopted, the range of wavelengths where the DLA transmission less than 0.8 is excluded from the forest.
2. Calculation of the flux-transmission field,  $\delta_q(\lambda)$ , for each quasar,  $q$ , at wavelength  $\lambda$  from the measured flux  $f_q(\lambda)$  (blue line of Fig 1):

$$\delta_q(\lambda) = \frac{f_q(\lambda)}{\bar{F}(\lambda)C_q(\lambda)} - 1. \quad (2.1)$$

Here  $\bar{F}(\lambda)$  is the mean transmitted flux fraction and  $C_q(\lambda)$  is the estimated unabsorbed

quasar continuum. The product  $\bar{F}(\lambda)C_q(\lambda)$  is shown as the red line in Fig. 1. As illustrated in Fig. 3, the  $\delta_q(\lambda)$  are defined on a wavelength grid with  $\Delta \log \lambda = 0.0001$  for BOSS and eBOSS and  $\Delta \lambda = 0.8 \text{\AA}$  for DESI. In the standard analysis (Sect. 2.4 of [9]), we use the  $\delta_q(\lambda)$  in the restframe wavelength range between the Ly $\alpha$  and Ly $\beta$  quasar lines:  $1040 < \lambda_{\text{RF}} < 1200 \text{\AA}$ . The product  $\bar{F}(\lambda)C_q(\lambda)$  is determined by fitting each forest to the mean forest spectrum modified by two free parameters per quasar reflecting the quasar brightness and spectral index. The mean forest spectrum is modified to include the effects of the wings of masked DLAs.

3. Use of a fiducial cosmological model to transform angular separations and redshift separations ( $\Delta z, \Delta \theta$ ) between pairs of flux-transmission field elements ( $\delta_q(\lambda), \delta_{q'}(\lambda')$ ) into co-moving distances ( $r_\perp, r_\parallel$ ) (Section 3.1 of [9]). Redshifts are derived from the observed wavelength  $\lambda$  assuming Ly $\alpha$  absorption.
4. Calculation of the forest auto-correlation function and quasar-forest cross-correlation in bins  $\Delta r_\perp = \Delta r_\parallel = 4h^{-1} \text{Mpc}$  (Sections 3.2 and 3.3 of [9]):

$$\xi_A^{\text{auto}} = \frac{\sum_{(i,j) \in A} w_i w_j \delta_i \delta_j}{\sum_{(i,j) \in A} w_i w_j} \quad \xi_A^{\text{cross}} = \frac{\sum_{(i,q) \in A} w_q w_i \delta_i}{\sum_{(i,q) \in A} w_q w_i}. \quad (2.2)$$

Here,  $i$  and  $j$  represent pixels on the  $\lambda$  grid of a given quasar. For the auto-correlation, the sum is over pairs ( $\delta_q(\lambda), \delta_{q'}(\lambda')$ ) in the  $(r_\perp, r_\parallel)$  bin  $A$ . The  $w_i$  are weights chosen to optimize the measurement by favoring measurements of low-noise and at high-redshift (where the correlation is expected to be highest). For the cross-correlation, the sum is over pairs of flux-transmission and quasars, ( $\delta_q(\lambda), q'$ ).

5. Calculation of the covariance matrix of the auto- and cross-correlations by sub-sampling (Sections 3.2 and 3.3 of [9]). The method consists of measuring the correlation functions in different regions of the sky and deducing the covariances from the variations between different regions.
6. Fit of the measured auto- and cross-correlations with a  $\Lambda$ CDM-based model (Sect. 4 of [9]) as described here in Sect. 3.

### 3 The model for correlations with HCDs

Following the procedure used in all BOSS, eBOSS, and DESI analyses, we model flux-flux and quasar-flux correlations with a biased power spectrum of the underlying  $\Lambda$ CDM matter power spectrum. For tracers  $i$  and  $j$  with biases and redshift-space distortion parameters ( $b_i, \beta_i$ ) and ( $b_j, \beta_j$ ) the spectrum is

$$\hat{P}(\mathbf{k}) = b_i b_j (1 + \beta_i \mu_k^2) (1 + \beta_j \mu_k^2) P_{\text{QL}}(\mathbf{k}) F_{\text{NL}}(\mathbf{k}) G(\mathbf{k}), \quad (3.1)$$

where the vector  $\mathbf{k} = (k_\parallel, k_\perp) = (k, \mu_k)$  of modulus  $k$ , has components along and across the line-of-sight,  $(k_\parallel, k_\perp)$ , with  $\mu_k = k_\parallel/k$ .  $P_{\text{QL}}$  is the linear  $\Lambda$ CDM power spectrum corrected for bulk flows around the BAO peak.  $F_{\text{NL}}$  models the effects on large- $\vec{k}$  modes of non-linear growth, Jeans smoothing, and line-of-sight broadening due to non-linear velocities and thermal broadening [53].



Finally,  $G(\mathbf{k})$  is a damping term that accounts for averaging of the correlation function in individual  $(r_{\parallel}, r_{\perp})$  bins.

For the auto-correlation, the main tracer is the Ly $\alpha$  absorption,  $i = j$ , denoted here by the pair  $(b_{\text{Ly}\alpha}, \beta_{\text{Ly}\alpha})$ . For the cross-correlation  $i \neq j$ , with the second pair  $(b_Q, \beta_Q)$ .

As described by MW12 and FM12, the broadening effect due to HCDs can be modeled with an effective scale-dependent bias:

$$\begin{cases} b'_{\text{Ly}\alpha} = b_{\text{Ly}\alpha} - b_{\text{HCD}} F_{\text{HCD}}^{\text{Voigt}}(k_{\parallel}) \\ b'_{\text{Ly}\alpha} \beta'_{\text{Ly}\alpha} = b_{\text{Ly}\alpha} \beta_{\text{Ly}\alpha} - b_{\text{HCD}} \beta_{\text{HCD}} F_{\text{HCD}}^{\text{Voigt}}(k_{\parallel}) \end{cases}, \quad (3.2)$$

where  $(b_{\text{Ly}\alpha}, \beta_{\text{Ly}\alpha})$  are the bias parameters of the IGM contribution to forest absorption, and  $(b_{\text{HCD}}, \beta_{\text{HCD}})$  are the bias parameters of the halos containing the HCDs. The function  $F_{\text{HCD}}^{\text{Voigt}}$  is

$$F_{\text{HCD}}^{\text{Voigt}}(k_{\parallel}) = \rho_{\text{HCD}} \int f(n) W(k_{\parallel}, n) dn. \quad (3.3)$$

Here  $\rho_{\text{HCD}}$  is the number density of HCDs per unit forest length,  $f(n)$  is the normalized column-density distribution of HCDs,  $n = \log N_{\text{HI}}$ , and  $W(k_{\parallel})$  is the Fourier transform of  $1 - V(\lambda)$  (defined in Eqn. A.7) where  $V$  is a Voigt profile illustrated in Fig. 2. This form of  $F_{\text{HCD}}^{\text{Voigt}}$  assumes  $b_{\text{HCD}}$  is independent of  $n$ . If not,  $b_{\text{HCD}}(n)$  must be included in the integral. Possible redshift dependencies of  $(b_{\text{HCD}}, \beta_{\text{HCD}})$  have also been ignored and we will assume throughout that referring these parameters to their values at the mean redshift is sufficient. With these restrictions, a demonstration of eqns. 3.2 and 3.3 is given in Appendix A.

The HCD density  $\rho_{\text{HCD}} f(n)$  is constrained by measurements in the DLA region [38],  $\log N_{\text{HI}}/1\text{cm}^{-2} > 20.3$ , and for  $\log N_{\text{HI}}/1\text{cm}^{-2} < 17.2$  [54]. For this study we use the calculated density of [55] shown in Fig. 4.

Figure 5 shows  $F_{\text{HCD}}^{\text{Voigt}}$  for different ranges of integration of the  $f(n)$  used in the production of the mocks. The function for the full range of column densities,  $17.2 < n < 22.5$ , is the solid green line. The two major contributors to this function are  $20.3 < n < 21.3$  and  $19.3 < n < 20.3$  with the highest column densities,  $21.3 < n < 22.5$ , having a minor importance. If one masks DLAs with  $n > 20.3$ , the solid grey line is the relevant function with the major contribution coming from the range  $19.3 < n < 20.3$ .

If  $f(n)$  is known (as for the mock data), equations 3.2 and 3.3 show that the power spectrum is determined by the combinations  $b_{\text{HCD}} \rho_{\text{HCD}}$  and  $b_{\text{HCD}} \beta_{\text{HCD}} \rho_{\text{HCD}}$ . For mock data, the known mean density is  $\rho_{\text{HCD}}(z_{\text{eff}} \approx 2.29) = 0.00158 \text{\AA}^{-1}$ , and by adopting this value fits of the correlation functions return values of  $(b_{\text{HCD}}, \beta_{\text{HCD}})$ . We will always place a strong prior on  $\beta_{\text{HCD}}$ , so fits of mock data can be considered to return simply a value of  $b_{\text{HCD}}$ .

For real data,  $f(n)$  is unknown for  $17.2 < \log N_{\text{HI}}/1\text{cm}^{-2} < 20$ . Because of this analyses have used a phenomenological form for  $F_{\text{HCD}}$ . The final eBOSS analysis [9] and the DESI analyses [10, 11] used

$$-b_{\text{HCD}} F_{\text{HCD}}^{\text{Voigt}} \rightarrow b_{\text{HCD}}^F \exp(-k_{\parallel} L_{\text{HCD}}). \quad (3.4)$$

Here  $b_{\text{HCD}}$  is the halo bias of HCDs, and  $b_{\text{HCD}}^F$  is the flux bias of HCDs. Since this model uses an exponential function, we call it the **Exp** model. Note that since  $b_{\text{HCD}} > 0$  and  $F_{\text{HCD}}^{\text{Voigt}}(k_{\parallel} = 0) > 0$ , then we must have  $b_{\text{HCD}}^F < 0$ . In previous BOSS, eBOSS and DESI papers that used the **Exp** model, our parameter  $b_{\text{HCD}}^F$  has been denoted simply as  $b_{\text{HCD}}$ .

In addition to the HCD effect on the bias, the power spectrum (3.1) is also cut off at high  $k_{\parallel}$  by the binning effect,  $G(k)$ , and non-linear effects,  $F_{\text{NL}}(k)$ , in the IGM [53] (This is

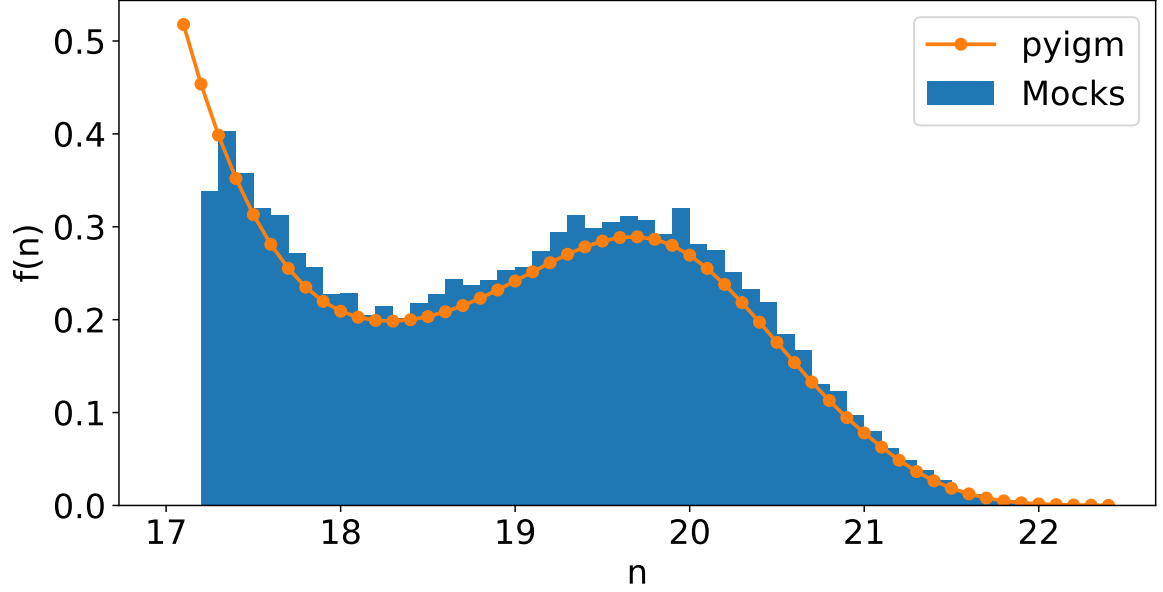


**Figure 4.** The  $N_{\text{HI}}$  distribution  $f(n = \log N_{\text{HI}}/1\text{cm}^{-2})$  that is used in our analysis. The orange curve shows the theoretical prediction from pyigm, and the blue points give the HCD distribution in our mocks.

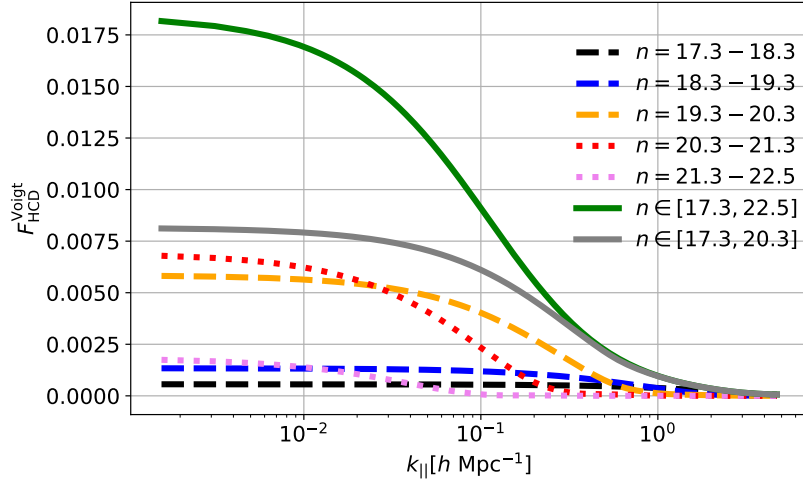


**Figure 5.** The function  $F_{\text{HCD}}^{\text{Voigt}}$  (equation 3.3) based on integration of HCDs with the distribution of  $N_{\text{HI}}$  over the ranges as labeled and assuming  $\rho_{\text{HCD}} = 0.00158 \text{\AA}^{-1}$ . The solid green line gives the complete  $F_{\text{HCD}}^{\text{Voigt}}$  if no DLAs are masked and the solid gray line the complete  $F_{\text{HCD}}^{\text{Voigt}}$  if all DLAs with  $\log N_{\text{HI}}/1\text{cm}^{-2} > 20.3$  are masked.

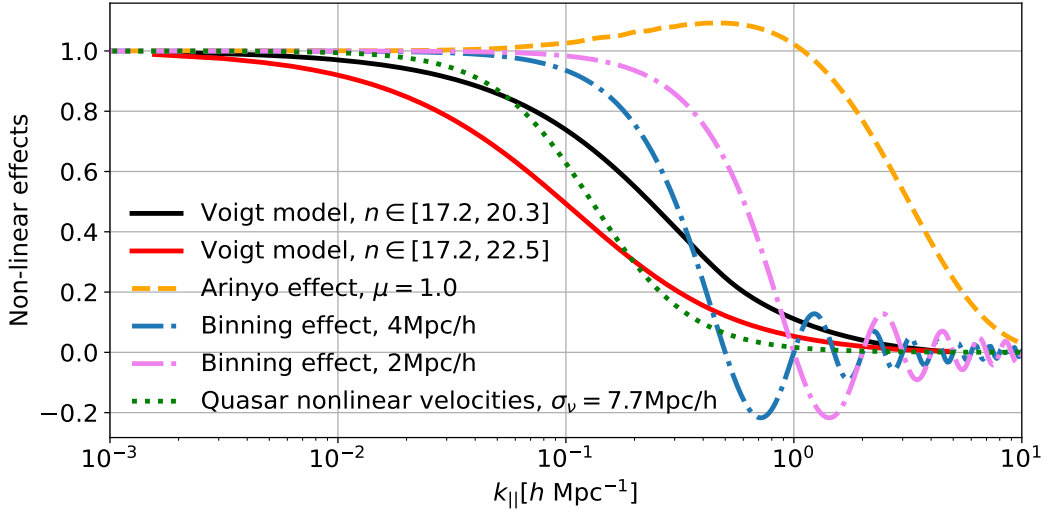


**Figure 6.** Effects of different terms that modify the Ly $\alpha$  forest power spectrum amplitude. The comparison of the Voigt model (Solid lines), the non-linear damping using the Arinyo model (Dashed line), the binning effect (Dotted-dashed lines), and the quasar nonlinear velocities (Dotted line).

modeled using the Arinyo model). For the cross-correlation, non-linear quasar velocities must also be taken into account for the real data (This effect is not included in the mock data). Figure 6 compares these effects. For the auto-correlation, we see that the HCD effect has a cutoff at the lowest values of  $k_{\parallel}$ , while for the cross-correlation quasar non-linear velocities have the cutoff at the lowest  $k_{\parallel}$  if  $n > 20.3$  DLAs are masked. The binning effect drops down quickly, thus masking the high- $k_{\parallel}$  tail of the HCD effect. The impact of the binning effect can be reduced by using smaller binsizes and this is investigated in the next section. For Ly $\alpha$ -quasar cross-correlations of real data, the quasar nonlinear velocities resulting in "Fingers-of-God" give a non-negligible cut-off, comparable to the HCD effect.

#### 4 Tests with mocks

To test the HCD model, we used the mock data sets described in Etourneau et al. [35]. In these mocks, the dominant IGM component of neutral hydrogen absorption was generated using Gaussian random fields followed by the application of the Fluctuating Gunn-Perterson Approximation (FGPA) [34] through equation 2.6 of [35]. HCDs were placed at density peaks according to the procedure of FM12 so as to produce an HCD bias of  $b_{\text{HCD}} = 2$  and  $\beta_{\text{HCD}} = 0.5$  [56]. The details of the insertion of HCDs and other astrophysical effects is described in Herrera-Alcantar et al. [57].

The mocks are generated to cover the SDSS-IV survey footprint and quasar density, with at the end, a catalog of 261854 quasars. The redshift and default distribution of  $n = \log N_{\text{HI}}$  of HCDs were those of the IGM physics package pyigm<sup>2</sup> [55, 58]. The pyigm distribution of  $\log N_{\text{HI}}$  is shown in Fig. 4. The number of HCDs per quasar and the density of HCDs are shown in Fig. 7. For a typical eBOSS quasar of redshift 2.5, there are  $\approx 0.6$  HCDs per quasar corresponding to density of  $\approx 0.0016(h^{-1}\text{Mpc})^{-1}$ .

<sup>2</sup><https://github.com/pyigm/pyigm>

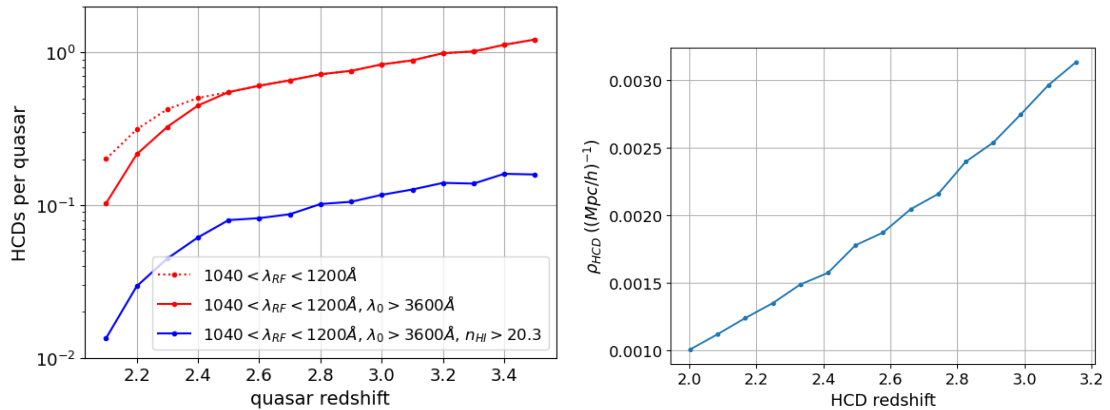


**Figure 7.** Statistics of HCDs as a function of redshift in the mock dataset: the number of HCDs per forest as a function of quasar redshift for the mock data (plot on the left); the density of HCDs as a function of redshift for the mock data (plot on the right).

In addition to mocks produced with the pygmy distribution of  $\log N_{\text{HI}}$ , in order to facilitate the testing of the HCD correlation model, special mock sets were generated with a unique value of  $\log N_{\text{HI}}$ . Sets were produced with the values  $n = 19.5, 20.0, 20.5$ , and  $21$ . For these mocks, correlation functions were computed with no DLAs masked. For mocks with the pygmy distribution  $f(n)$ , fits were performed both with and without masking DLAs, the former corresponding to  $n \in [17.2, 20.3]$  and the latter to  $n \in [17.2, 22.5]$ .

The complete auto- and cross-correlation functions for stacks of 10 Ly $\alpha$  mocks are shown in Figure 8 for the mock sets with unique values of  $n$ .

For the fits of mock data, we have 6 free parameters  $\{\alpha_{\parallel}, \alpha_{\perp}, b_{\eta\text{Ly}\alpha}, \beta_{\text{Ly}\alpha}, b_{\eta\text{HCD}}, \beta_{\text{HCD}}\}$  in the fitting of the auto-correlation function, where  $b_{\eta\text{Ly}\alpha} = b_{\text{Ly}\alpha} \times \beta_{\text{Ly}\alpha}$  and  $b_{\eta\text{HCD}} = b_{\text{HCD}} \times \beta_{\text{HCD}}$ . As in du Mas des Bourboux et al. [9] we find that the fits do not constrain well the parameter  $\beta_{\text{HCD}}$ , so we use a Gaussian prior  $\beta_{\text{HCD}} = 0.5 \pm 0.09$ .

For the cross-correlation, we have one more free parameter,  $\Delta r_{\parallel}$ , that models any systematic shift in quasar redshifts relative to that of the  $\lambda$  grid. The parameters  $b_{\text{QSO}}$  and  $\beta_{\text{QSO}}$  are fixed because they are not significantly constrained by the cross-only fits and we do not perform joint auto-cross fits.

#### 4.1 Fits with the Voigt model

The best-fit bias parameters,  $(b_{\text{HCD}}, \beta_{\text{HCD}}, b_{\eta\text{Ly}\alpha}^{\eta}, \beta_{\text{Ly}\alpha})$ , for stacks of 10 mocks for the Voigt model are shown in Table 1 and compared with the expected values in Fig. 9. Table 3 and Table 4 shows the results for all the fitted parameters. The values of  $b_{\text{HCD}}$  are all within two standard deviations of the expected value,  $b_{\text{HCD}} = 2$ . The values for  $(b_{\eta\text{Ly}\alpha}^{\eta}, \beta_{\text{Ly}\alpha})$  are stable with respect to changes in the distribution of  $\log N_{\text{HI}}$ . We note however, that fits with  $2h^{-1}\text{Mpc}$  binning (Table 5) yield somewhat smaller values for  $b_{\text{HCD}}$ . The BAO parameters  $(\alpha_{\perp}, \alpha_{\parallel})$  are consistent with the expected values of unity.

The poor fits of the mocks with  $n = 21$  may be due to various reasons. One potential explanation suggests that it is due to the distortions of the quasar continuum fitting in the Ly $\alpha$  analysis pipeline, as HCDs with such wide damping absorption wings will have a significant distortion on the continuum fitting. These distortions can be further investigated in future analysis using quasar true continuum.

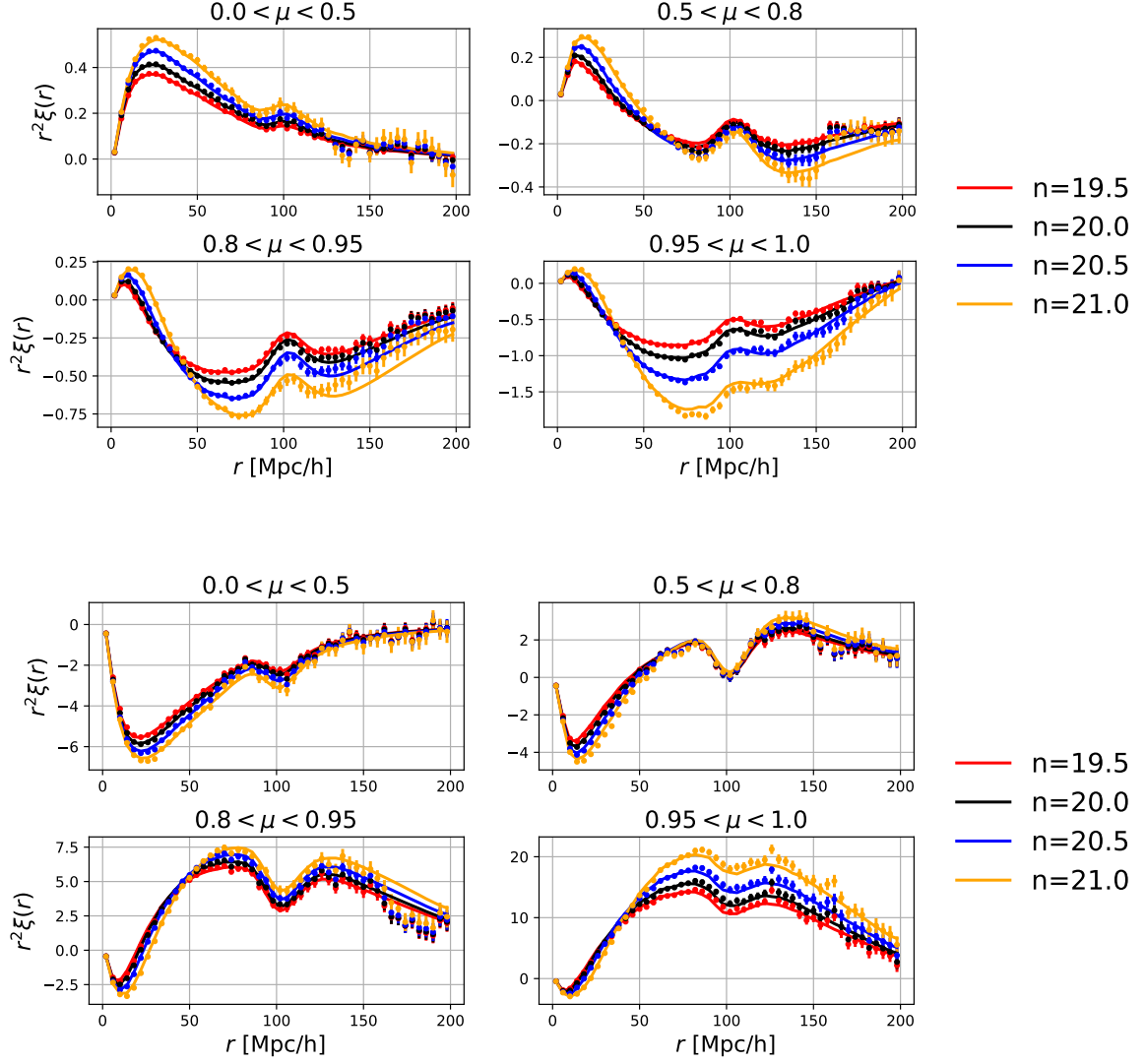


**Figure 8.** The Ly $\alpha$  auto-correlation function (top four panels) and Ly $\alpha$ -quasar cross-correlation (bottom four panels), for mock data. The points of different colors give the measured correlation for mocks with HCDs with unique column densities  $\log N_{\text{HI}}/\text{cm}^{-2} = 19.5, 20, 20.5, 21$ , and the curves give the best fit models using the Voigt model, in four wedges of  $|\mu| = |\frac{r_{\perp}}{r}|$ . The fitted range is chosen as  $r \in [20, 180]h^{-1}\text{Mpc}$ .

Figure 10 shows the correlated constraints on  $\{b_{\text{eff,LY}\alpha}, b_{\eta, \text{LY}\alpha}, b_{\text{HCD}}\}$  for the Voigt model fits of the auto-correlations. We use the bias determining the monopole  $b_{\text{eff,LY}\alpha} = b_{\text{LY}\alpha}(1 + \frac{2}{3}\beta_{\text{LY}\alpha} + \frac{1}{5}\beta_{\text{LY}\alpha}^2)^{1/2}$  instead of  $b_{\text{LY}\alpha}$  since it is less correlated with  $\beta_{\text{LY}\alpha}$  [35]. We do not show  $\beta_{\text{HCD}}$  since it is mostly determined by priors.

## 4.2 Comparison with the Exp model

Fits were performed the Exp model on the mock data with the pygim distribution  $f(n)$  with both masking and no-masking. Compared to the Voigt model, the Exp model has one additional free parameter  $L_{\text{HCD}}$ .

	$b_{\text{HCD}}$	$\beta_{\text{HCD}}$	$b_{\eta, \text{Ly}\alpha}$	$\beta_{\text{Ly}\alpha}$
$\text{Ly}\alpha \times \text{Ly}\alpha$				
$n = 19.5$	$1.95 \pm 0.292$	$0.48 \pm 0.09$	$-0.206 \pm 0.002$	$1.61 \pm 0.04$
$n = 20.0$	$2.13 \pm 0.157$	$0.48 \pm 0.08$	$-0.204 \pm 0.003$	$1.6 \pm 0.05$
$n = 20.5$	$2.2 \pm 0.092$	$0.5 \pm 0.07$	$-0.201 \pm 0.003$	$1.57 \pm 0.06$
$n = 21.0$	$1.92 \pm 0.052$	$0.75 \pm 0.05$	$-0.187 \pm 0.003$	$1.33 \pm 0.05$
$n \in [17.2, 20.3]$	$1.93 \pm 0.346$	$0.48 \pm 0.09$	$-0.206 \pm 0.001$	$1.64 \pm 0.04$
$n \in [17.2, 22.5]$	$1.82 \pm 0.146$	$0.48 \pm 0.08$	$-0.205 \pm 0.002$	$1.64 \pm 0.04$
$\text{Ly}\alpha \times \text{QSO}$				
$n = 19.5$	$2.3 \pm 0.488$	$0.51 \pm 0.09$	$-0.194 \pm 0.004$	$1.67 \pm 0.08$
$n = 20.0$	$2.64 \pm 0.427$	$0.53 \pm 0.09$	$-0.191 \pm 0.006$	$1.78 \pm 0.13$
$n = 20.5$	$2.59 \pm 0.275$	$0.56 \pm 0.08$	$-0.19 \pm 0.007$	$1.89 \pm 0.18$
$n = 21.0$	$2.12 \pm 0.138$	$0.63 \pm 0.08$	$-0.191 \pm 0.007$	$1.67 \pm 0.14$
$n \in [17.2, 20.3]$	$2.2 \pm 0.49$	$0.51 \pm 0.09$	$-0.193 \pm 0.003$	$1.63 \pm 0.05$
$n \in [17.2, 22.5]$	$2.46 \pm 0.387$	$0.53 \pm 0.09$	$-0.191 \pm 0.004$	$1.78 \pm 0.11$

**Table 1.** Best-fit Voigt model values of the four bias parameters for stacks of 10 mocks. The parameters are shown for the different distributions of  $n = \log N_{\text{HI}}$  described in the first column. The complete sets of best-fit parameters are shown in Tables 3 and 4.

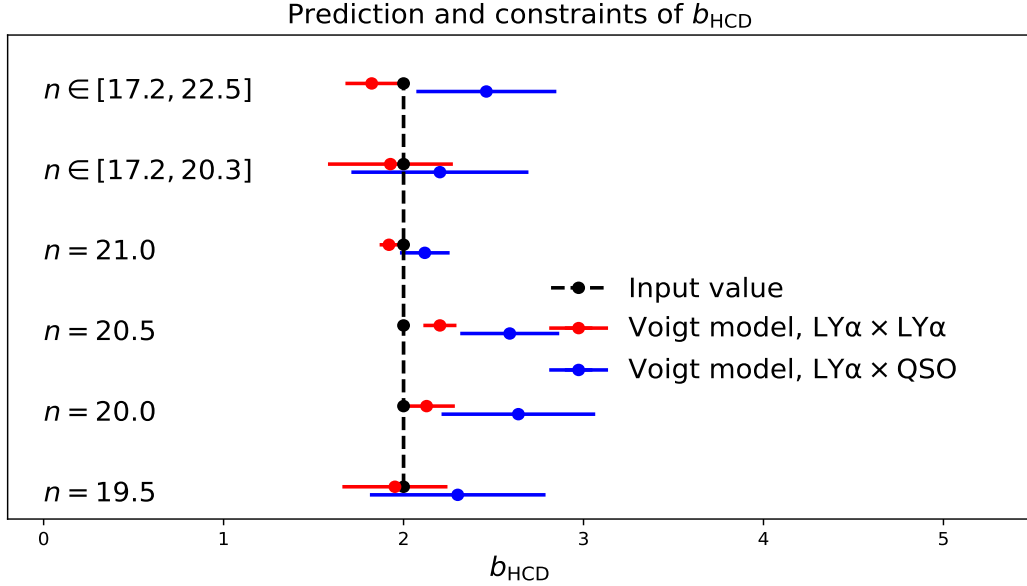


**Figure 9.** Measurements of  $b_{\text{HCD}}$  using the Voigt model for mocks with different distributions of  $\log N_{\text{HI}}$ . The black points show the true value of  $b_{\text{HCD}} = 2.0$ . The red points and blue points are fitted from auto- and cross-correlations respectively.

	$b_{\text{HCD}}$ Voigt model	$b_{\text{HCD}}^F$ Exp model	$L_{\text{HCD}}$ Exp model	$\beta_{\text{HCD}}$	$b_{\eta, \text{Ly}\alpha}$	$\beta_{\text{Ly}\alpha}$
Ly $\alpha$ $\times$ Ly $\alpha$ Mocks binsize = $4h^{-1}\text{Mpc}$ $n \in [17.2, 20.3]$	$1.93 \pm 0.346$			$0.48 \pm 0.09$	$-0.206 \pm 0.001$	$1.64 \pm 0.04$
$n \in [17.2, 22.5]$	$1.82 \pm 0.146$	$-0.008 \pm 0.004$	$7.86 \pm 6.64$	$0.49 \pm 0.09$	$-0.209 \pm 0.002$	$1.56 \pm 0.04$
		$-0.026 \pm 0.004$	$9.5 \pm 2.56$	$0.48 \pm 0.08$	$-0.205 \pm 0.002$	$1.64 \pm 0.04$
				$0.48 \pm 0.09$	$-0.208 \pm 0.002$	$1.58 \pm 0.05$
Ly $\alpha$ $\times$ Ly $\alpha$ Mocks binsize = $2h^{-1}\text{Mpc}$ $n \in [17.2, 20.3]$	$1.58 \pm 0.355$			$0.46 \pm 0.09$	$-0.202 \pm 0.001$	$1.56 \pm 0.03$
$n \in [17.2, 22.5]$	$1.66 \pm 0.149$	$-0.004 \pm 0.002$	$15.1 \pm 11.4$	$0.48 \pm 0.09$	$-0.206 \pm 0.001$	$1.48 \pm 0.02$
		$-0.024 \pm 0.004$	$9.12 \pm 2.79$	$0.47 \pm 0.09$	$-0.202 \pm 0.002$	$1.58 \pm 0.04$
				$0.47 \pm 0.09$	$-0.205 \pm 0.002$	$1.53 \pm 0.05$
Ly $\alpha$ $\times$ Ly $\alpha$ DR16 binsize = $4h^{-1}\text{Mpc}$ $n \in [17.2, 20.3]$	$7.3 \pm 0.611$			$0.67 \pm 0.08$	$-0.179 \pm 0.004$	$1.71 \pm 0.11$
$n \in [17.2, 22.5]$	$4.79 \pm 0.326$	$-0.105 \pm 0.022$	$2.28 \pm 0.63$	$0.53 \pm 0.08$	$-0.175 \pm 0.013$	$3.23 \pm 1.26$
		$-0.139 \pm 0.02$	$2.59 \pm 0.52$	$0.67 \pm 0.08$	$-0.189 \pm 0.005$	$1.84 \pm 0.14$
				$0.51 \pm 0.08$	$-0.173 \pm 0.013$	$5.25 \pm 3.29$
Ly $\alpha$ $\times$ QSO Mocks binsize = $4h^{-1}\text{Mpc}$ $n \in [17.2, 20.3]$	$2.2 \pm 0.49$			$0.51 \pm 0.09$	$-0.193 \pm 0.003$	$1.63 \pm 0.05$
$n \in [17.2, 22.5]$	$2.46 \pm 0.387$	$-0.077 \pm 0.024$	$2.56 \pm 1.22$	$0.51 \pm 0.07$	$-0.169 \pm 0.015$	$2.83 \pm 0.92$
		$-0.082 \pm 0.06$	$4.97 \pm 4.64$	$0.53 \pm 0.09$	$-0.191 \pm 0.004$	$1.78 \pm 0.11$
				$0.52 \pm 0.09$	$-0.176 \pm 0.036$	$2.83 \pm 1.74$
Ly $\alpha$ $\times$ QSO Mocks binsize = $2h^{-1}\text{Mpc}$ $n \in [17.2, 20.3]$	$2.21 \pm 0.49$			$0.51 \pm 0.09$	$-0.191 \pm 0.003$	$1.65 \pm 0.06$
$n \in [17.2, 22.5]$	$2.5 \pm 0.385$	$-0.016 \pm 0.005$	$32.3 \pm 33.3$	$0.51 \pm 0.09$	$-0.2 \pm 0.003$	$1.6 \pm 0.08$
		$-0.074 \pm 0.012$	$5.87 \pm 1.69$	$0.53 \pm 0.09$	$-0.189 \pm 0.004$	$1.79 \pm 0.11$
				$0.52 \pm 0.08$	$-0.18 \pm 0.009$	$1.6 \pm 0.31$
Ly $\alpha$ $\times$ QSO DR16 binsize = $4h^{-1}\text{Mpc}$ $n \in [17.2, 20.3]$	$3.78 \pm 1.92$			$0.51 \pm 0.09$	$-0.237 \pm 0.014$	$1.91 \pm 0.21$
$n \in [17.2, 22.5]$	$-0.424 \pm 1.4$	$-0.034 \pm 0.024$	$0.95 \pm 2.87$	$0.52 \pm 0.09$	$-0.228 \pm 0.016$	$1.91 \pm 0.33$
		$-0.047 \pm 0.027$	$-0.01 \pm 1.66$	$0.5 \pm 0.09$	$-0.27 \pm 0.018$	$1.56 \pm 0.16$
				$0.51 \pm 0.09$	$-0.231 \pm 0.019$	$1.91 \pm 0.34$

**Table 2.** Best-fit Voigt and Exp model values of the bias parameters for stacks of 10 mocks and for the eBOSS dr16 data. For the Voigt model, the HCD bias parameters are  $(b_{\text{HCD}}, \beta_{\text{HCD}})$  and for the Exp model the bias parameters are  $(b_{\text{HCD}}^F, L_{\text{HCD}}, \beta_{\text{HCD}})$ . The parameters are shown for the two pygmy distributions of  $n = \log N_{\text{HI}}$  described in the first column and for two bins sizes. The complete sets of best-fit parameters are shown in Tables 3 and 4.

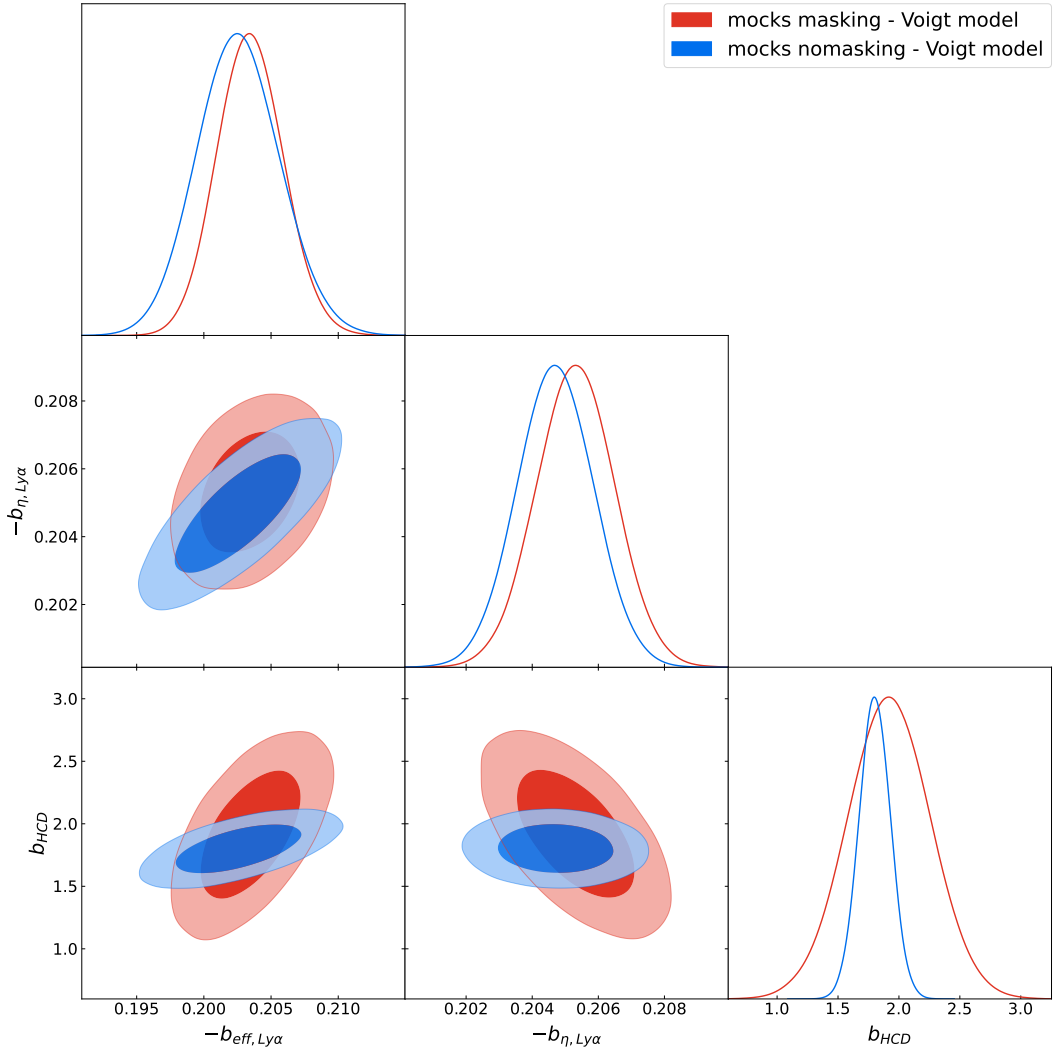


**Figure 10.** Correlated constraints for the Ly $\alpha$  parameters constraints  $\{b_{\text{eff}, \text{Ly}\alpha}, b_{\eta, \text{Ly}\alpha}, b_{\text{HCD}}\}$  using the Voigt model fits of the auto-correlation.

Table 2 shows the best-fit bias parameters for the Voigt and Exp models. The complete set of fit parameters is shown in Table 4 where we see that both models give acceptable values of  $\chi^2$  and the difference between them is not sufficient to establish the superiority of one over the other.

The functions  $b'(k_{\parallel})$  and  $b'(k_{\parallel})\beta'(k_{\parallel})$  are shown in Figure 11. The Voigt and Exp model functions are very similar except at large  $k_{\parallel}$  where the other damping components (Fig. 6) are important.

Figure 12 shows the correlated constraints of the Ly $\alpha$  bias parameters  $\{b_{\text{eff}, \text{Ly}\alpha}, b_{\eta, \text{Ly}\alpha}, b_{\text{HCD}}^F, L_{\text{HCD}}\}$  for the Exp model. For masked mocks, the constraints on the two HCD parameters are weak:  $b_{\text{HCD}}^F = -0.008 \pm 0.004$  and  $L_{\text{HCD}} = 7.8 \pm 6.6$ . The one parameter of the Voigt model is determined with better precision:  $b_{\text{HCD}} = 1.93 \pm 0.35$ . For the unmasked mocks, both models give significant non-zero values for the HCD bias.

The values of IGM parameters  $(b_{\text{Ly}\alpha}^{\eta}, \beta_{\text{Ly}\alpha})$  are comparable for the masking and no-



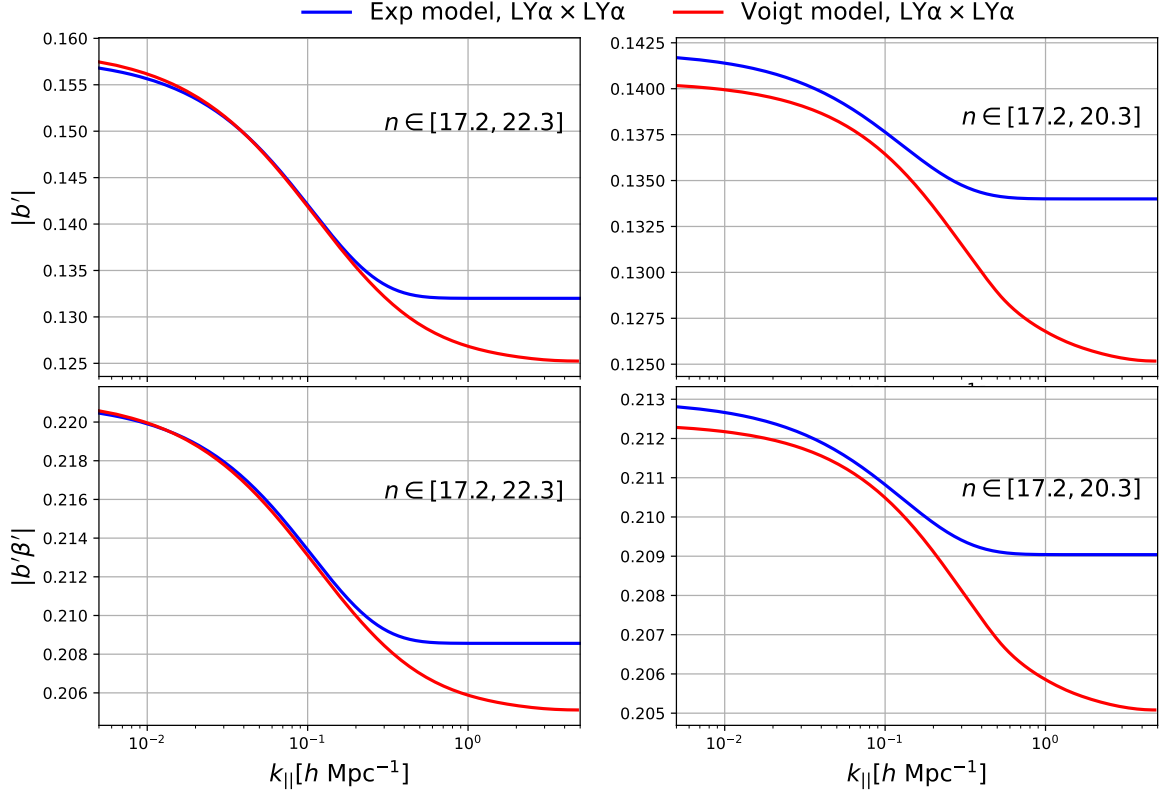


**Figure 11.** The scale-dependent biases  $b'/\beta'$  and  $b'$  from eqn. 3.2 as a function of  $k_{\parallel}$  for the **Voigt** model (blue) and from eqn. 3.4 for the **Exp** model (red). The biases are shown for the full range of  $N_{\text{HI}}$  (left) and for masked DLAs (right) as determined by fitting the auto-correlation function.

masking cases.

A comparison of the **Voigt** and **Exp** models for the auto-correlation fits of the IGM bias parameters  $\{|b_{\text{eff}, \text{LY}\alpha}|, |b_{\eta, \text{LY}\alpha}|\}$  is shown in Figure 13. The **Voigt** model gives tighter constraints on both IGM parameters.

## 5 Fits with eBOSS data

Application of the Voigt model to real data involves two difficulties. First, the fits require knowledge of the density of HCDs,  $\rho f(n)$ . While this is known for the mock data, it can only be estimated for the data using the known distribution of column densities for DLAs. Second, if the identified DLAs are masked, it is necessary to understand the detection efficiency of DLAs and model the effects of unmasked DLAs, as well as the impact of masking incorrectly non-DLA structures.

Two strategies can address these two problems. First, one could simply not mask any identified DLAs and model the full HCD distribution using the pyigm distribution normalized so as to reproduce the distribution of DLAs measured in high signal-to-noise forests. An alternative strategy would be to mask only DLAs found in high-S/N forests and model the correlations with with two  $F_{\text{HCD}}$ 's, one for the masked high-S/N forests and one for the

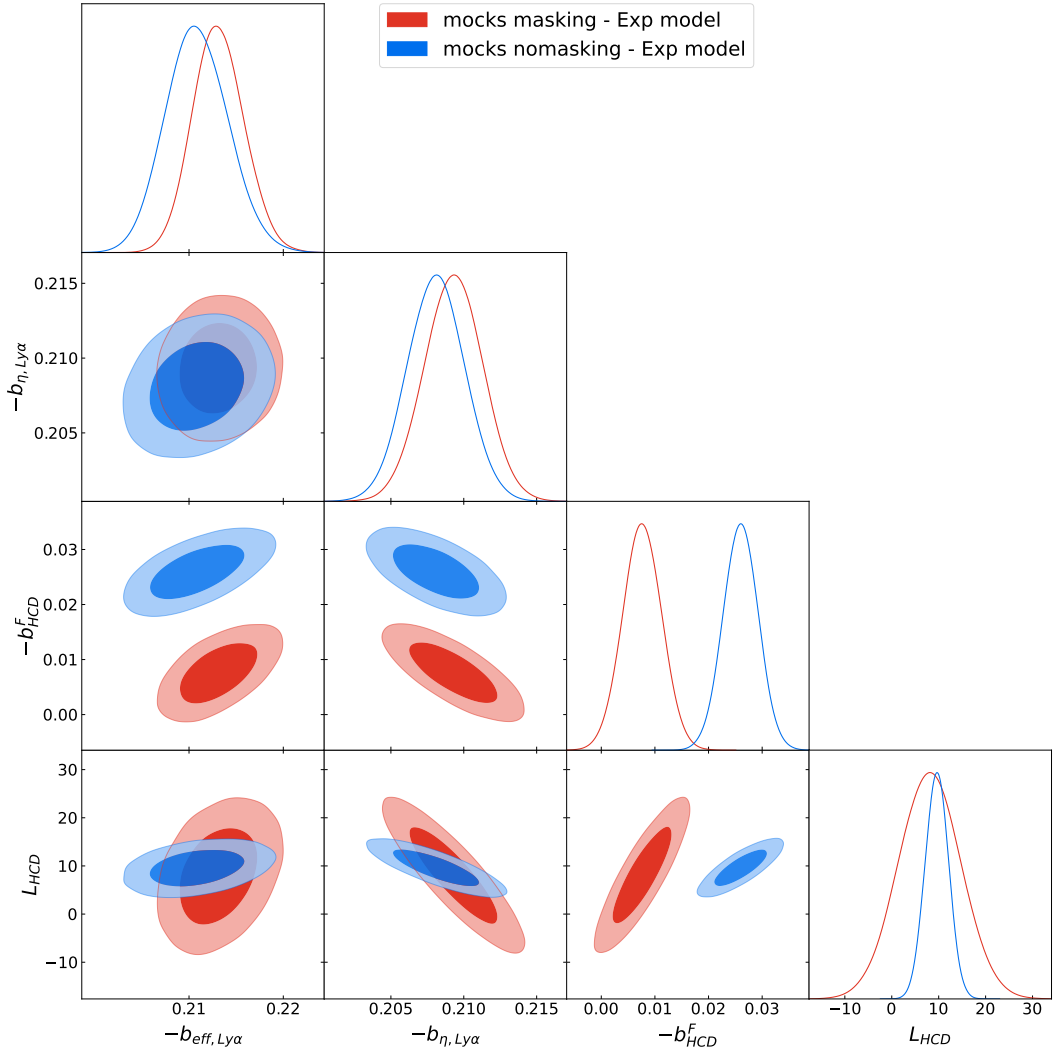


**Figure 12.** For the **Exp** model, the correlated constraints for the  $\text{Ly}\alpha$  parameters  $\{b_{\text{eff}, \text{Ly}\alpha}, b_{\eta, \text{Ly}\alpha}, b_{\text{HCD}}^F, L_{\text{HCD}}\}$ . The one and two standard deviation contours are calculated assuming a Gaussian likelihood so for the marginally measured parameter,  $L_{\text{HCD}}$ , the two-standard deviation curves are not realistic.

unmasked low-S/N forests. This strategy has not yet been implemented, so here we adopt the strategy of masking DLA's identified in [9].

Compared to the mock data used in the previous section, fits with real data need 7 additional free parameters to account for effects not included in the mocks: five to characterize the different metal absorption lines overlapping with the  $\text{Ly}\alpha$  absorption in real data, and two parameters that model the sky subtraction residuals [9].

These parameters are not expected to be degenerate with the HCD parameters: the major metal parameters are well determined by peaks in the correlations at small  $r_{\perp}$  and the sky subtraction parameter is determined by excess correlations at  $r_{\parallel} = 0$ . For the cross correlation, we also fit a parameter,  $\sigma_v$  taking into account the quasar velocity distribution parameter. As indicated by Fig. 6, this gives a lower cutoff in  $k_{\parallel}$  if the DLAs are masked, making the HCD effect uncertain.

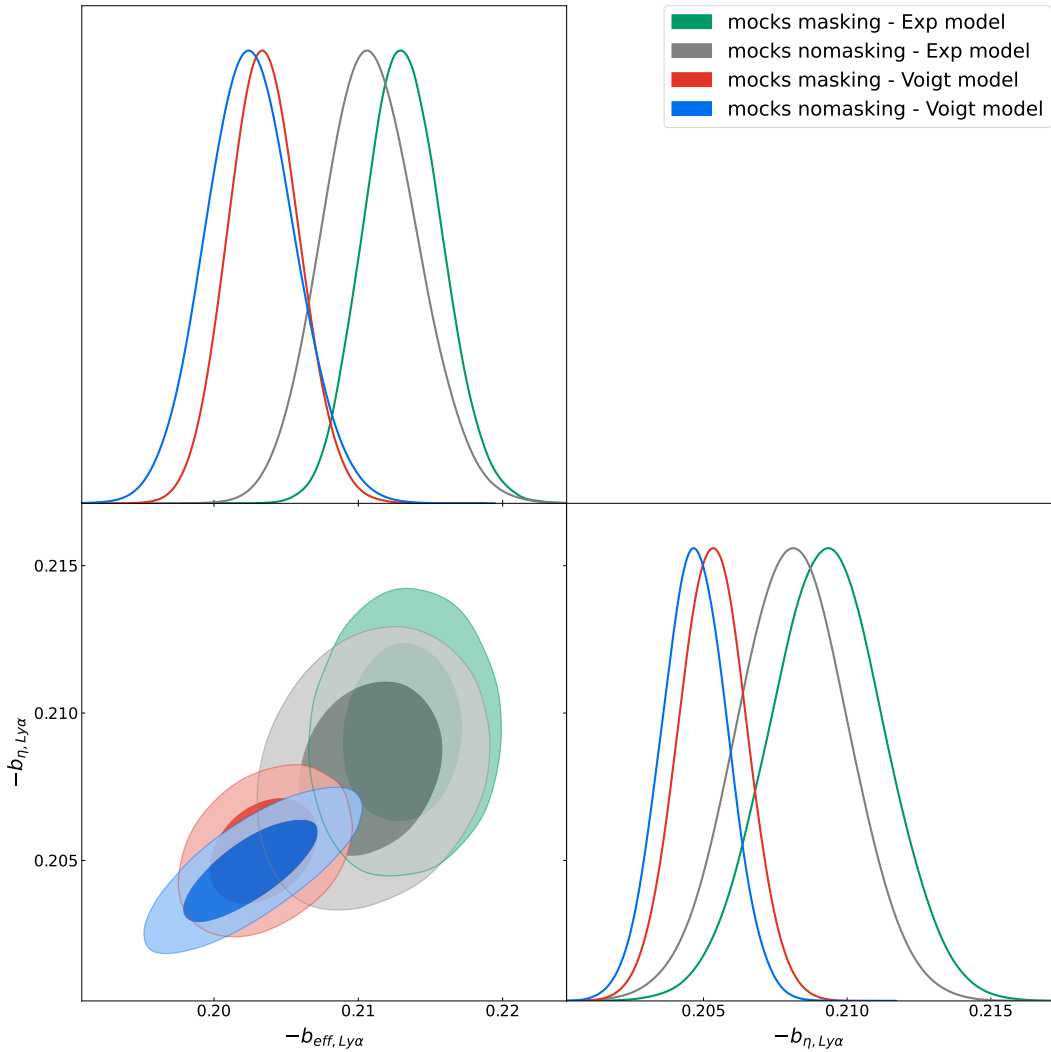


**Figure 13.** The comparison of the constraints on the Ly $\alpha$  IGM bias parameters  $\{b_{\text{eff}, \text{Ly}\alpha}, b_{\eta, \text{Ly}\alpha}\}$  between the Voigt model and the Exp model fits of the auto-correlation.

The fits in the final eBOSS analysis [9] used the **Exp** model but assumed  $L_{\text{HCD}} = 10h^{-1}\text{Mpc}$ . As with the mock analysis, here we take  $L_{\text{HCD}}$  as a free parameter. Fits were performed both by masking identified DLAs and without masking. The parameter  $\beta_{\text{HCD}}$  is mainly determined by the input Gaussian prior  $\beta_{\text{HCD}} = 0.5 \pm 0.09$ . For the Voigt fits,  $\rho f(n)$  was taken to be that of pyigm.

Table 2 gives the values for the bias parameters, and Table 6 shows the results for all the fitted parameters. For the auto-correlation, the derived values of  $b_{\text{HCD}}$  and  $b_{\text{HCD}}^F$  are significantly larger than those found for the mocks. With no masking we find  $b_{\text{HCD}} = 7.3 \pm 0.6$  for DR16 data compared to  $1.93 \pm 0.35$  for the mocks. With masking we find  $b_{\text{HCD}} = 4.8 \pm 0.63$  for DR16 data compared to  $1.82 \pm 0.15$  for the mocks. The value of  $L_{\text{HCD}}$  is very low (less than the  $r_{\parallel}$  bin size) and does not change when there is no masking.

These facts suggest that the HCDs in the data are either more numerous or more biased than in the mocks or that there are additional effects in the data that smear the correlations

in the radial direction, which are then modeled with the HCD parameters.

## 6 Conclusion and Discussion

We have applied the **Voigt** model proposed in MW12 and FM12 to characterize the effect of HCDs on the  $\text{Ly}\alpha$  forest correlation function and power spectrum. This model is based on the Voigt absorption profile that parametrizes the damping wings of HCDs, and takes into account the HI column density probability distribution of HCDs, and the biases of the halos containing the HCD's. Note that in this work, we do not account for the redshift dependence. This approximation is appropriate for the current analysis, where the  $\text{Ly}\alpha$  forest correlation functions are measured at an effective redshift. However, a more detailed treatment of the redshift dependence will be necessary in future analyses.

We performed a suite of verifications of the model, based on the fitting to  $\text{Ly}\alpha$  forest correlations, computed from mocks with different HI column density probability distributions of HCDs. The fitted values of  $b_{\text{HCD}}$  are generally consistent with the expected value  $b_{\text{HCD}} = 2$ , confirming the validity of the model. Compared with the adhoc **Exp** model, the **Voigt** model gives comparable  $\chi^2$ , with a smaller uncertainty for  $b_{\eta\text{Ly}\alpha}$  and  $\beta_{\text{Ly}\alpha}$ .

Application of the **Voigt** model to real data will be challenging because of uncertainties in the HCD content and bias and the effects of masking false DLA detections. If it can be understood, the HI column density distribution in the range of  $17 < n < 20$ , could also potentially be constrained with this model, which is difficult to measure from direct observation. However, the large value of  $b_{\text{HCD}}$  fit with real data suggests that other smearing effects are present in the data. Fortunately, the eBOSS DR16 data confirms that the modeling of HCDs does not affect the measurement of BAO significantly. Validation analyses based on DESI data will be further investigated for this model.

## 7 Data availability

The data points corresponding to each figure in this paper can be accessed in the Zenodo repository at <https://doi.org/10.5281/zenodo.15591451>.

## A Derivation of the Voigt and Exp models

Following the work of MW11 and FM12, we derive here eqn. 3.2, found in this appendix as eqns. A.29 and A.30. The motivation is to correct some minor errors in these papers and in [50].

We divide the absorption caused by neutral hydrogen in two groups: the absorption  $\tau_\alpha$  caused by the Lyman- $\alpha$  forest in the Intergalactic Medium (IGM) and the absorption  $\tau_H$  caused by High Column Density systems (HCDs) in the vicinity of galaxies. The total transmitted flux fraction  $F_T$  due to absorption at the position  $x$  will be the product of both:

$$F_T(x) = F_\alpha(x)F_H(x) \quad (\text{A.1})$$

$$= \overline{F_\alpha} [1 + \delta_\alpha(x)] \overline{F_H} [1 + \delta_H(x)] \quad (\text{A.2})$$

$$= \overline{F_T} [1 + \delta_T(x)] .$$

Since  $\delta_\alpha$  and  $\delta_H$  are correlated, the relation between the mean fluxes is:

$$\overline{F_T} = \langle F_T \rangle = \overline{F_\alpha} \overline{F_H} [1 + C] , \quad (\text{A.3})$$

where we have introduced  $C = \langle \delta_\alpha(x) \delta_H(x) \rangle$ .

The fluctuations in the total transmitted flux fraction are then:

$$1 + \delta_T(x) = \frac{1}{1 + C} [1 + \delta_\alpha(x)] [1 + \delta_H(x)] , \quad (\text{A.4})$$

or in other words,

$$\delta_T = \frac{\delta_\alpha + \delta_H + \delta_\alpha \delta_H - C}{1 + C} . \quad (\text{A.5})$$

FM12 estimate  $C \approx 0.003$  and for the rest of the discussion we will make the approximation  $C = 0$  and ignore the second order term  $\delta_\alpha \delta_H$ , obtaining the simple relation

$$\delta_T \approx \delta_\alpha + \delta_H . \quad (\text{A.6})$$

If we had not made this approximation we should not obtain that the total flux bias is the sum of that due to the IGM and that due to the HCDs, since this ignores  $C$  and the other higher order terms that would modify even the linear bias parameters.

### A.1 Absorption due to the Voigt profile

The absorption at radial position  $x$  due to the presence of a HCD of column density  $N_{\text{HI}}$  at  $x'$  is

$$1 - F_H(x) = [1 - V(x' - x, n)] , \quad (\text{A.7})$$

where  $V(x' - x, n = \log N_{\text{HI}})$  is a Voigt profile for a column density  $N_{\text{HI}}$ , normalized at  $V = 1$  at large  $x' - x$ .<sup>3</sup> The probability of having a HCD at a given position  $x'$  and column density  $N_{\text{HI}}$  is  $\rho_{\text{HCD}} f(n) dx' dn$  where  $\rho_{\text{HCD}}$  is the density of HCDs and  $f(n)$  is the normalized distribution of  $n = \log N_{\text{HI}}$ . In a region with a linear overdensity  $\delta_L(x')$ , the probability is enhanced

$$p(n, x') = \rho_{\text{HCD}} f(n) [1 + b_{\text{HCD}}(n) \delta_L(x')] , \quad (\text{A.8})$$

where we have introduced the linear bias of the halos hosting HCDs, in principle a function of column density  $b_{\text{HCD}}(n)$ .

Using this probability we can write the integrals:

$$1 - F_H(x) = \int dx' \int dn p(n, x') [1 - V(x' - x, n)] , \quad (\text{A.9})$$

and compute the value of  $\overline{F_H}$  using the value of  $p(n, x')$  at  $\delta_L = 0$ :

$$1 - \overline{F_H} = \rho_{\text{HCD}} \int dn f(n) W(n) , \quad (\text{A.10})$$

where we have defined

$$W(n) = \int dx' [1 - V(x' - x, n)] , \quad (\text{A.11})$$

the equivalent width of the Voigt profile in comoving units (not in  $\text{\AA}$ ).

---

<sup>3</sup>This definition of  $V$  corresponds to  $(1 - V)$  of FM12

We can now describe the fluctuation in HCD absorption as:

$$\delta_H(x) = \frac{F_H(x) - \overline{F_H}}{\overline{F_H}} \quad (\text{A.12})$$

$$\begin{aligned} &= -\frac{1}{\overline{F_H}} \int dx' \int dn [p(n, x') - \rho_{\text{HCD}} f(n)] [1 - V(x' - x, n)] \\ &= -\frac{\rho_{\text{HCD}}}{\overline{F_H}} \int dn f(n) b_{\text{HCD}}(n) \int dx' \delta_L(x') [1 - V(x' - x, n)] . \end{aligned} \quad (\text{A.13})$$

The expression is clearer in Fourier space, since the convolution becomes a product of Fourier modes:

$$\delta_H(k_{\parallel}) = -\rho_{\text{HCD}} \frac{\delta_L(k_{\parallel})}{\overline{F_H}} \int dn f(n) b_{\text{HCD}}(n) W(k_{\parallel}, n) , \quad (\text{A.14})$$

where  $W(k_{\parallel}, n)$  is the Fourier transform of  $[1 - V(x, n)]$ .

## A.2 Linear bias of HCD absorption

On very large scales, larger than the typical size of DLAs, we should recover a linear bias relation. To distinguish between the linear bias of the HCD systems ( $b_{\text{HCD}}$ ) and the linear bias of the absorption caused by these, we will refer to the latter as  $b_{\text{HCD}}^F$ , i.e.,  $\delta_H(k) = b_{\text{HCD}}^F \delta_L(k)$ . Using eqn. A.14 we get:

$$b_{\text{HCD}}^F = \frac{\rho_{\text{HCD}}}{\overline{F_H}} \int dn f(n) b_{\text{HCD}}(n) W(n) , \quad (\text{A.15})$$

where we have used the fact that

$$\begin{aligned} \lim_{k_{\parallel} \rightarrow 0} W(k_{\parallel}, n) &= \lim_{k_{\parallel} \rightarrow 0} \int dx e^{ik_{\parallel}x} [1 - V(x, n)] \\ &= \int dx [1 - V(x, n)] = W(n) . \end{aligned} \quad (\text{A.16})$$

For a  $n$ -independent bias  $b_{\text{HCD}}(N) = b_{\text{HCD}}$ , using eqn. A.10 this gives

$$b_{\text{HCD}}^F = b_{\text{HCD}} \frac{1 - \overline{F_H}}{\overline{F_H}} . \quad (\text{A.17})$$

## A.3 Relation with the Exponential model

In the Exp model used in previous eBOSS [9] and DESI [59] analyses, we describe the contamination as

$$\delta_H(k) = b_{\text{HCD}}^F \exp[-L_{\text{HCD}} k_{\parallel}] \delta_L(k) , \quad (\text{A.18})$$

where  $b_{\text{HCD}}^F$  is the large-scale bias. Using eqns. A.14 and A.15, we can write a similar equation for the Voigt model:

$$\delta_H(k) = b_{\text{HCD}}^F F_V(k_{\parallel}) \delta_L(k) , \quad (\text{A.19})$$

where  $b_{\text{HCD}}^F$  is the linear bias discussed above, and we have introduced

$$F_V(k_{\parallel}) = \frac{\int dn f(n) b_{\text{HCD}}(n) W(k_{\parallel}, n)}{\int dn f(n) b_{\text{HCD}}(n) W(n)} . \quad (\text{A.20})$$

The correspondence with  $F_{\text{HCD}}^{\text{Voigt}}$  in eqn. 3.3 is

$$b_{\text{HCD}} F_{\text{HCD}}^{\text{Voigt}}(k_{\parallel}) = b_{\text{HCD}}^F F_V(k_{\parallel}) \quad (\text{A.21})$$

#### A.4 Redshift space distortions

To include redshift-space distortions, we replace  $b_{\text{HCD}}$  with  $b_{\text{HCD}} + f\mu_k^2$  where  $f \approx 1$  (no argument  $n$ ) is the linear growth rate and  $\mu_k = k_{\parallel}/k$  with  $k_{\parallel}$  being the component of  $k$  along the line of sight.

$$\delta_H(k, \mu_k) = \rho_{\text{HCD}} \frac{\delta_L(k)}{\overline{F}_H} \int dn f(n) [b_{\text{HCD}}(n) + f\mu_k^2] W(k_{\parallel}, n) . \quad (\text{A.22})$$

Similarly to how we have computed  $b_{\text{HCD}}^F$  above, we can now compute the low- $k$  limit for  $\mu_k = 1$ :

$$b_{\text{HCD}}^F [1 + \beta_{\text{HCD}}] = \lim_{k \rightarrow 0} \frac{\delta_H(k, \mu_k = 1)}{\delta_L(k)} \quad (\text{A.23})$$

$$= \frac{\rho_{\text{HCD}}}{\overline{F}_H} \int dn f(n) [b_{\text{HCD}}(n) + f] W(n) \quad (\text{A.24})$$

$$= b_{\text{HCD}}^F + f \frac{1 - \overline{F}_H}{\overline{F}_H} . \quad (\text{A.25})$$

From this, one can obtain the value of  $\beta_{\text{HCD}}$ :

$$\beta_{\text{HCD}} = f \frac{1}{b_{\text{HCD}}^F} \frac{1 - \overline{F}_H}{\overline{F}_H} . \quad (\text{A.26})$$

Whenever we have  $b_{\text{HCD}}(n) = b_{\text{HCD}}$  we can further simplify the expression:

$$\beta_{\text{HCD}} = \frac{f}{b_{\text{HCD}}} . \quad (\text{A.27})$$

#### A.5 Contaminated Kaiser model

Assuming again that  $\delta_T = \delta_{\alpha} + \delta_H$  and  $b_{\text{HCD}}^F(n) = b_{\text{HCD}}^F$ , it is easy to see that

$$\frac{\delta_T(k, \mu_k)}{\delta_L(k)} = [b_{\text{Ly}\alpha} + b_{\text{HCD}}^F F_V(k_{\parallel})] + [b_{\text{Ly}\alpha} \beta_{\text{Ly}\alpha} + b_{\text{HCD}}^F \beta_{\text{HCD}} F_V(k_{\parallel})] \mu_k^2 , \quad (\text{A.28})$$

i.e.,

$$b_T(k_{\parallel}) = b_{\text{Ly}\alpha} + b_{\text{HCD}}^F F_V(k_{\parallel}) \quad (\text{A.29})$$

and

$$b_T^{\eta}(k_{\parallel}) = b_{\text{Ly}\alpha}^{\eta} + b_{\text{HCD}}^{\eta} F_V(k_{\parallel}) , \quad (\text{A.30})$$

where we have used the *velocity gradient bias*

$$b_X^{\eta} = \frac{b_X \beta_X}{f} . \quad (\text{A.31})$$

Equations A.29 and A.30 are equivalent to equation 3.2 with the identification  $b_{\text{HCD}}^F F_V(k_{\parallel}) = b_{\text{HCD}} F_{\text{HCD}}^{\text{Voigt}}(k_{\parallel})$ .

## A.6 Comparison to MW11

Eq. (B.1) of MW11 shows the power spectrum of HCD contamination:

$$P_H(k, \mu) = (b_h + \mu^2)^2 P_L(k) \left( \tilde{W}_2(k_{\parallel}) \right)^2, \quad (\text{A.32})$$

where the authors assume that all HCDs have the same bias and that  $f = 1$ . Their  $b_h$  corresponds to our  $b_{\text{HCD}}$ .

The authors define  $\tilde{W}_2(k_{\parallel})$  in Eq. (B.2) as:

$$\tilde{W}_2(k_{\parallel}) = \int dN f(N) W(N, k), \quad (\text{A.33})$$

(although they use  $\tilde{d}(k_{\parallel})$  to refer to  $W(k, N)$ ). Their  $f(N)$  corresponds to our  $\rho_{\text{HCD}} f(n)$

On the other hand, our model predicts that the power of HCD contamination should be:

$$P_H(k, \mu) = \left( \frac{b_H}{b_h} \right)^2 (b_h + f\mu^2)^2 P_L(k) F_V^2(k_{\parallel}). \quad (\text{A.34})$$

If we assume again that  $b_h(N) = b_h$ , we can simplify the equation using

$$\frac{b_H}{b_h} F_V(k_{\parallel}) = \frac{1 - \overline{F_H}}{\overline{F_H}} F_V(k) \quad (\text{A.35})$$

$$\begin{aligned} &= \frac{1 - \overline{F_H}}{\overline{F_H}} \frac{\int dN f(N) W(k, N)}{\int dN f(N) W(N)} \\ &= \frac{1}{\overline{F_H}} \int dN f(N) W(k, N) \\ &= \frac{1}{\overline{F_H}} \tilde{W}_2(k). \end{aligned} \quad (\text{A.36})$$

It appears that MW11 missed a factor of  $1/\overline{F_H}$  in their calculations. This number is very close to one, so the difference is minor.

## A.7 Comparison to FM12

Eq. (4.25) in FM12 shows the relation between the cross-correlation term  $\xi_{\alpha H}^V$  taking into account the Voigt profile, compared to the same term without the Voigt profile  $\xi_{\alpha H}$ . The authors used  $V(N)$  to refer to the absorption, i.e., what here we call  $1 - V(N)$ .

If we do the Fourier transform, and rewrite it in terms of comoving coordinates (and not velocities), we can rewrite the equation as:

$$P_{\alpha H}^V(k, \mu) = F_V(k_{\parallel}) P_{\alpha H}(k, \mu), \quad (\text{A.37})$$

with

$$F_V(k_{\parallel}) = \frac{\int dN f(N) W(N, k)}{\int dN f(N) W(N)}. \quad (\text{A.38})$$

This is similar to our Eq. A.20, but only if one assumes  $b_h(N) = b_h$ . This is not important when analyzing mocks, but in general the halo bias could be a function of column density.



	Ly $\alpha$ $\times$ Ly $\alpha$	Ly $\alpha$ $\times$ Ly $\alpha$	Ly $\alpha$ $\times$ Ly $\alpha$	Ly $\alpha$ $\times$ Ly $\alpha$
$n$	19.5	20.0	20.5	21.0
$N_{\text{mocks}}$	10	10	10	10
$z_{\text{eff}}$	2.29	2.29	2.29	2.29
$[r_{\text{min}}, r_{\text{max}}](h^{-1}\text{Mpc})$	[20,180]	[20,180]	[20,180]	[20,180]
$\chi^2$	1583.58	1584.23	1583.63	1682.56
$N_{\text{data}}$	1574	1574	1574	1574
$N_{\text{par}}$	6	6	6	6
$P$	0.39	0.38	0.39	0.02
$\alpha_{\parallel}$	$1.01 \pm 0.009$	$1.01 \pm 0.009$	$1.01 \pm 0.01$	$1.0 \pm 0.01$
$\alpha_{\perp}$	$0.998 \pm 0.013$	$1.0 \pm 0.015$	$1.0 \pm 0.017$	$1.01 \pm 0.019$
$b_{\eta, \text{Ly}\alpha}$	$-0.206 \pm 0.002$	$-0.204 \pm 0.003$	$-0.201 \pm 0.003$	$-0.187 \pm 0.003$
$\beta_{\text{Ly}\alpha}$	$1.61 \pm 0.04$	$1.6 \pm 0.05$	$1.57 \pm 0.06$	$1.33 \pm 0.05$
$b_{\text{HCD}}$	$1.95 \pm 0.292$	$2.13 \pm 0.157$	$2.2 \pm 0.092$	$1.92 \pm 0.052$
$\beta_{\text{HCD}}$	$0.48 \pm 0.09$	$0.48 \pm 0.08$	$0.5 \pm 0.07$	$0.75 \pm 0.05$
	Ly $\alpha$ $\times$ QSO	Ly $\alpha$ $\times$ QSO	Ly $\alpha$ $\times$ QSO	Ly $\alpha$ $\times$ QSO
$z_{\text{eff}}$	2.29	2.29	2.29	2.29
$[r_{\text{min}}, r_{\text{max}}](h^{-1}\text{Mpc})$	[40,180]	[40,180]	[40,180]	[40,180]
$\chi^2$	2994.79	3029.07	3056.4	3074.56
$N_{\text{data}}$	3030	3030	3030	3030
$N_{\text{par}}$	7	7	7	7
$P$	0.64	0.47	0.33	0.25
$\alpha_{\parallel}$	$1.0 \pm 0.009$	$1.0 \pm 0.01$	$1.0 \pm 0.01$	$0.998 \pm 0.01$
$\alpha_{\perp}$	$1.0 \pm 0.011$	$1.0 \pm 0.012$	$1.0 \pm 0.013$	$1.0 \pm 0.014$
$b_{\eta, \text{Ly}\alpha}$	$-0.194 \pm 0.004$	$-0.191 \pm 0.006$	$-0.19 \pm 0.007$	$-0.191 \pm 0.007$
$\beta_{\text{Ly}\alpha}$	$1.67 \pm 0.08$	$1.78 \pm 0.13$	$1.89 \pm 0.18$	$1.67 \pm 0.14$
$b_{\text{HCD}}$	$2.3 \pm 0.488$	$2.64 \pm 0.427$	$2.59 \pm 0.275$	$2.12 \pm 0.138$
$\beta_{\text{HCD}}$	$0.51 \pm 0.09$	$0.53 \pm 0.09$	$0.56 \pm 0.08$	$0.63 \pm 0.08$
$\Delta r_{\parallel, \text{QSO}} (h^{-1}\text{Mpc})$	$0.41 \pm 0.17$	$0.36 \pm 0.18$	$0.27 \pm 0.2$	$0.19 \pm 0.22$

**Table 3.** Best fit parameters for stack of 10 mocks created with HCDs with the column densities  $n = \log N_{\text{HI}} = 19.5, 20.0, 20.5, 21.0$ , using the Voigt model, for Ly $\alpha$  auto-correlation function and Ly $\alpha$ -quasar cross-correlation.

## A.8 Comparison to Rogers et al. (2018)

Eq. (3) in Rogers et al. [50] shows the estimate for  $F_V(k_{\parallel})$  to be:

$$F_V(k) = \int dN f(N) W(N, k) . \quad (\text{A.39})$$

This is significantly different than our results, since they ignore the normalization factor, so their  $F_V(k)$  does not go to 1 on large scales, and it goes instead to  $1 - \overline{F_H}$ .

The results would be equivalent to [48] if  $b_{\text{HCD}}$  in Eq. (2) of [50] meant the halo bias (our  $b_{\text{HCD}}$ ), not the absorption bias (our  $b_{\text{HCD}}^F$ ) as stated.

## B Complete results of fits

Tables 3, 4, 5, and 6 give the complete results of fits on the mocks and dr16 eBOSS data.

Model Masking	Exp Yes $\text{Ly}\alpha \times \text{Ly}\alpha$	Voigt Yes $\text{Ly}\alpha \times \text{Ly}\alpha$	Exp No $\text{Ly}\alpha \times \text{Ly}\alpha$	Voigt No $\text{Ly}\alpha \times \text{Ly}\alpha$
$N_{\text{mocks}}$	10	10	10	10
$z_{\text{eff}}$	2.29	2.29	2.29	2.29
$[r_{\text{min}}, r_{\text{max}}](h^{-1}\text{Mpc})$	[20,180]	[20,180]	[20,180]	[20,180]
$\chi^2$	1522.52	1523.24	1533.47	1534.13
$N_{\text{data}}$	1574	1574	1574	1574
$N_{\text{par}}$	7	6	7	6
$P$	0.79	0.79	0.72	0.72
$\alpha_{\parallel}$	$1.01 \pm 0.009$	$1.01 \pm 0.009$	$1.0 \pm 0.009$	$1.0 \pm 0.009$
$\alpha_{\perp}$	$0.98 \pm 0.013$	$0.98 \pm 0.013$	$0.984 \pm 0.015$	$0.984 \pm 0.015$
$b_{\eta, \text{Ly}\alpha}$	$-0.209 \pm 0.002$	$-0.206 \pm 0.001$	$-0.208 \pm 0.002$	$-0.205 \pm 0.002$
$\beta_{\text{Ly}\alpha}$	$1.56 \pm 0.04$	$1.64 \pm 0.04$	$1.58 \pm 0.05$	$1.64 \pm 0.04$
$\beta_{\text{HCD}}$	$0.49 \pm 0.09$	$0.48 \pm 0.09$	$0.48 \pm 0.09$	$0.48 \pm 0.08$
$b_{\text{HCD}}$		$1.93 \pm 0.346$		$1.82 \pm 0.146$
$b_{\text{HCD}}^F$	$-0.008 \pm 0.004$		$-0.026 \pm 0.004$	
$L_{\text{HCD}}$	$7.86 \pm 6.64$		$9.5 \pm 2.56$	
	$\text{Ly}\alpha \times \text{QSO}$	$\text{Ly}\alpha \times \text{QSO}$	$\text{Ly}\alpha \times \text{QSO}$	$\text{Ly}\alpha \times \text{QSO}$
$z_{\text{eff}}$	2.29	2.29	2.29	2.29
$[r_{\text{min}}, r_{\text{max}}](h^{-1}\text{Mpc})$	[40,180]	[40,180]	[40,180]	[40,180]
$\chi^2$	3133.7	3138.72	3110.47	3112.57
$N_{\text{data}}$	3030	3030	3030	3030
$N_{\text{par}}$	8	7	8	7
$P$	0.08	0.07	0.13	0.13
$\alpha_{\parallel}$	$1.0 \pm 0.009$	$1.0 \pm 0.009$	$1.0 \pm 0.01$	$1.0 \pm 0.009$
$\alpha_{\perp}$	$1.0 \pm 0.011$	$1.0 \pm 0.011$	$0.996 \pm 0.012$	$0.997 \pm 0.012$
$b_{\eta, \text{Ly}\alpha}$	$-0.169 \pm 0.015$	$-0.193 \pm 0.003$	$-0.176 \pm 0.034$	$-0.191 \pm 0.004$
$\beta_{\text{Ly}\alpha}$	$2.83 \pm 0.92$	$1.63 \pm 0.05$	$2.52 \pm 1.68$	$1.78 \pm 0.11$
$\beta_{\text{HCD}}$	$0.51 \pm 0.07$	$0.51 \pm 0.09$	$0.52 \pm 0.09$	$0.53 \pm 0.09$
$b_{\text{HCD}}$		$2.2 \pm 0.49$		$2.46 \pm 0.387$
$b_{\text{HCD}}^F$	$-0.077 \pm 0.024$		$-0.082 \pm 0.057$	
$L_{\text{HCD}}$	$2.56 \pm 1.22$		$4.96 \pm 4.44$	
$\Delta r_{\parallel, \text{QSO}} (h^{-1}\text{Mpc})$	$0.2 \pm 0.17$	$0.2 \pm 0.17$	$0.18 \pm 0.19$	$0.19 \pm 0.19$

**Table 4.** Best fit parameters for stack of 10 mocks created with HCDs with pygmy column densities, using the **Voigt** and **Exp** models, for  $\text{Ly}\alpha$  auto-correlation function and  $\text{Ly}\alpha$ -quasar cross-correlation, respectively.

## Acknowledgments

This material is based upon work supported by the U.S. Department of Energy (DOE), Office of Science, Office of High-Energy Physics, under Contract No. DE-AC02-05CH11231, and by the National Energy Research Scientific Computing Center, a DOE Office of Science User Facility under the same contract. Additional support for DESI was provided by the U.S. National Science Foundation (NSF), Division of Astronomical Sciences under Contract No. AST-0950945 to the NSF’s National Optical-Infrared Astronomy Research Laboratory; the Science and Technology Facilities Council of the United Kingdom; the Gordon and Betty Moore Foundation; the Heising-Simons Foundation; the French Alternative Energies and Atomic Energy Commission (CEA); the National Council of Humanities, Science and Technology of Mexico (CONAHCYT); the Ministry of Science, Innovation and Uni-

Model	Exp	Voigt	Exp	Voigt
Masking	Yes	Yes	No	No
	$\text{Ly}\alpha \times \text{Ly}\alpha$	$\text{Ly}\alpha \times \text{Ly}\alpha$	$\text{Ly}\alpha \times \text{Ly}\alpha$	$\text{Ly}\alpha \times \text{Ly}\alpha$
$N_{\text{mocks}}$	10	10	10	10
$z_{\text{eff}}$	2.29	2.29	2.29	2.29
$[r_{\text{min}}, r_{\text{max}}](h^{-1}\text{Mpc})$	[20,180]	[20,180]	[20,180]	[20,180]
$\chi^2$	6340.93	6344.04	6308.51	6309.75
$N_{\text{data}}$	6048	6048	6048	6048
$N_{\text{par}}$	7	6	7	6
$P$	0.0	0.0	0.01	0.01
$\alpha_{\parallel}$	$1.0 \pm 0.009$	$1.0 \pm 0.009$	$1.0 \pm 0.009$	$1.0 \pm 0.009$
$\alpha_{\perp}$	$0.984 \pm 0.014$	$0.983 \pm 0.014$	$0.984 \pm 0.015$	$0.984 \pm 0.015$
$b_{\eta, \text{Ly}\alpha}$	$-0.206 \pm 0.001$	$-0.202 \pm 0.001$	$-0.205 \pm 0.002$	$-0.202 \pm 0.002$
$\beta_{\text{Ly}\alpha}$	$1.48 \pm 0.02$	$1.56 \pm 0.03$	$1.53 \pm 0.05$	$1.58 \pm 0.04$
$\beta_{\text{HCD}}$	$0.48 \pm 0.09$	$0.46 \pm 0.09$	$0.47 \pm 0.09$	$0.47 \pm 0.09$
$b_{\text{HCD}}$		$1.58 \pm 0.355$		$1.66 \pm 0.149$
$b_{\text{HCD}}^F$	$-0.004 \pm 0.002$		$-0.024 \pm 0.004$	
$L_{\text{HCD}}$	$15.09 \pm 11.39$		$9.12 \pm 2.79$	
	$\text{Ly}\alpha \times \text{QSO}$	$\text{Ly}\alpha \times \text{QSO}$	$\text{Ly}\alpha \times \text{QSO}$	$\text{Ly}\alpha \times \text{QSO}$
$z_{\text{eff}}$	2.29	2.29	2.29	2.29
$[r_{\text{min}}, r_{\text{max}}](h^{-1}\text{Mpc})$	[40,180]	[40,180]	[40,180]	[40,180]
$\chi^2$	12209.06	12215.94	12290.08	12292.53
$N_{\text{data}}$	12092	12092	12092	12092
$N_{\text{par}}$	8	7	8	7
$P$	0.21	0.2	0.09	0.09
$\alpha_{\parallel}$	$1.0 \pm 0.009$	$1.0 \pm 0.01$	$1.01 \pm 0.01$	$1.0 \pm 0.01$
$\alpha_{\perp}$	$0.999 \pm 0.012$	$0.999 \pm 0.012$	$0.996 \pm 0.013$	$0.997 \pm 0.013$
$b_{\eta, \text{Ly}\alpha}$	$-0.2 \pm 0.003$	$-0.191 \pm 0.003$	$-0.18 \pm 0.009$	$-0.189 \pm 0.004$
$\beta_{\text{Ly}\alpha}$	$1.6 \pm 0.08$	$1.65 \pm 0.06$	$2.3 \pm 0.31$	$1.79 \pm 0.11$
$\beta_{\text{HCD}}$	$0.51 \pm 0.09$	$0.51 \pm 0.09$	$0.52 \pm 0.08$	$0.53 \pm 0.09$
$b_{\text{HCD}}$		$2.21 \pm 0.49$		$2.5 \pm 0.385$
$b_{\text{HCD}}^F$	$-0.016 \pm 0.005$		$-0.074 \pm 0.012$	
$L_{\text{HCD}}$	$32.34 \pm 33.3$		$5.87 \pm 1.69$	
$\Delta r_{\parallel, \text{QSO}}(h^{-1}\text{Mpc})$	$0.49 \pm 0.18$	$0.49 \pm 0.18$	$0.52 \pm 0.19$	$0.53 \pm 0.19$

**Table 5.** Same as Table 4 except now with binning size of  $2h^{-1}\text{Mpc}$ .

versities of Spain (MICIU/AEI/10.13039/501100011033), and by the DESI Member Institutions: <https://www.desi.lbl.gov/collaborating-institutions>. Any opinions, findings, and conclusions or recommendations expressed in this material are those of the author(s) and do not necessarily reflect the views of the U. S. National Science Foundation, the U. S. Department of Energy, or any of the listed funding agencies.

The authors are honored to be permitted to conduct scientific research on I’oligam Du’ag (Kitt Peak), a mountain with particular significance to the Tohono O’odham Nation.

Ting Tan thanks the French CNRS International PhD program for its support. The authors thank Andreu Font-Ribera for his contribution of writing Appendix A of this paper. We also thank Julien Guy for his contribution to the derivation of the model included in this paper.

Model Masking	Exp Yes	Voigt Yes	Exp No	Voigt No
	$\text{Ly}\alpha \times \text{Ly}\alpha$	$\text{Ly}\alpha \times \text{Ly}\alpha$	$\text{Ly}\alpha \times \text{Ly}\alpha$	$\text{Ly}\alpha \times \text{Ly}\alpha$
$z_{\text{eff}}$	2.29	2.29	2.29	2.29
$[r_{\text{min}}, r_{\text{max}}](h^{-1}\text{Mpc})$	[10,180]	[10,180]	[10,180]	[10,180]
$\chi^2$	1576.22	1624.34	1594.96	1630.65
$N_{\text{data}}$	1590	1590	1590	1590
$N_{\text{par}}$	14	13	14	13
$P$	0.49	0.2	0.36	0.17
$\alpha_{\parallel}$	$1.05 \pm 0.034$	$1.04 \pm 0.033$	$1.04 \pm 0.034$	$1.04 \pm 0.033$
$\alpha_{\perp}$	$0.981 \pm 0.042$	$0.985 \pm 0.041$	$0.974 \pm 0.044$	$0.973 \pm 0.044$
$b_{\eta, \text{Ly}\alpha}$	$-0.175 \pm 0.013$	$-0.179 \pm 0.004$	$-0.173 \pm 0.013$	$-0.189 \pm 0.005$
$\beta_{\text{Ly}\alpha}$	$3.23 \pm 1.26$	$1.71 \pm 0.11$	$5.25 \pm 3.29$	$1.84 \pm 0.14$
$\beta_{\text{HCD}}$	$0.53 \pm 0.08$	$0.67 \pm 0.08$	$0.51 \pm 0.08$	$0.67 \pm 0.08$
$b_{\text{HCD}}$		$7.3 \pm 0.611$		$4.79 \pm 0.326$
$b_{\text{HCD}}^F$	$-0.105 \pm 0.022$		$-0.139 \pm 0.02$	
$L_{\text{HCD}}$	$2.28 \pm 0.63$		$2.59 \pm 0.52$	
	$\text{Ly}\alpha \times \text{QSO}$	$\text{Ly}\alpha \times \text{QSO}$	$\text{Ly}\alpha \times \text{QSO}$	$\text{Ly}\alpha \times \text{QSO}$
$z_{\text{eff}}$	2.29	2.29	2.29	2.29
$[r_{\text{min}}, r_{\text{max}}](h^{-1}\text{Mpc})$	[10,180]	[10,180]	[10,180]	[10,180]
$\chi^2$	3220.27	3221.4	3219.44	3224.94
$N_{\text{data}}$	3180	3180	3180	3180
$N_{\text{par}}$	13	12	13	12
$P$	0.25	0.25	0.25	0.24
$\alpha_{\parallel}$	$1.06 \pm 0.032$	$1.06 \pm 0.032$	$1.05 \pm 0.034$	$1.05 \pm 0.034$
$\alpha_{\perp}$	$0.932 \pm 0.039$	$0.933 \pm 0.039$	$0.948 \pm 0.042$	$0.947 \pm 0.042$
$b_{\eta, \text{Ly}\alpha}$	$-0.228 \pm 0.016$	$-0.237 \pm 0.014$	$-0.231 \pm 0.019$	$-0.27 \pm 0.018$
$\beta_{\text{Ly}\alpha}$	$1.91 \pm 0.33$	$1.91 \pm 0.21$	$1.92 \pm 0.34$	$1.56 \pm 0.16$
$\beta_{\text{HCD}}$	$0.52 \pm 0.09$	$0.51 \pm 0.09$	$0.51 \pm 0.09$	$0.5 \pm 0.09$
$b_{\text{HCD}}$		$3.78 \pm 1.92$		$-0.424 \pm 1.4$
$b_{\text{HCD}}^F$	$-0.034 \pm 0.024$		$-0.047 \pm 0.027$	
$L_{\text{HCD}}$	$0.95 \pm 2.87$		$-0.01 \pm 1.66$	
$\Delta r_{\parallel, \text{QSO}} (h^{-1}\text{Mpc})$	$0.15 \pm 0.13$	$0.19 \pm 0.13$	$0.19 \pm 0.13$	$0.21 \pm 0.13$
$\sigma_v (h^{-1}\text{Mpc})$	$8.94 \pm 0.69$	$8.94 \pm 0.55$	$9.79 \pm 0.78$	$10.3 \pm 0.84$

**Table 6.** Best fit parameters for eBOSS DR16 data, using the **Voigt** model and the **Exp** model, for  $\text{Ly}\alpha$  auto-correlation function and  $\text{Ly}\alpha$ -quasar cross-correlation, respectively.

## References

- [1] Busca, N. G., T. Delubac, J. Rich, et al. Baryon acoustic oscillations in the  $\text{Ly}\alpha$  forest of BOSS quasars. *Astronomy & Astrophysics*, 552:A96, 2013. [arXiv:astro-ph.CO/1211.2616](#).
- [2] Slosar, A., V. Iršič, D. Kirkby, et al. Measurement of baryon acoustic oscillations in the Lyman- $\alpha$  forest fluctuations in BOSS data release 9. *Journal of Cosmology and Astroparticle Physics*, 2013:026, 2013. [arXiv:astro-ph.CO/1301.3459](#).
- [3] Delubac, T., J. E. Bautista, N. G. Busca, et al. Baryon acoustic oscillations in the  $\text{Ly}\alpha$  forest of BOSS DR11 quasars. *Astronomy & Astrophysics*, 574:A59, 2015. [arXiv:astro-ph.CO/1404.1801](#).
- [4] Bautista, J. E., N. G. Busca, J. Guy, et al. Measurement of baryon acoustic oscillation correlations at  $z = 2.3$  with SDSS DR12  $\text{Ly}\alpha$ -Forests. *Astronomy & Astrophysics*, 603:A12, 2017. [arXiv:astro-ph.CO/1702.00176](#).

- [5] de Sainte Agathe, V., C. Balland, H. du Mas des Bourboux, et al. Baryon acoustic oscillations at  $z = 2.34$  from the correlations of Ly $\alpha$  absorption in eBOSS DR14. *Astronomy & Astrophysics*, 629:A85, 2019. [arXiv:astro-ph.CO/1904.03400](#).
- [6] Font-Ribera, A., D. Kirkby, N. Busca, et al. Quasar-Lyman  $\alpha$  forest cross-correlation from BOSS DR11: Baryon Acoustic Oscillations. *Journal of Cosmology and Astroparticle Physics*, 2014:027, 2014. [arXiv:astro-ph.CO/1311.1767](#).
- [7] du Mas des Bourboux, H., J.-M. Le Goff, M. Blomqvist, et al. Baryon acoustic oscillations from the complete SDSS-III Ly $\alpha$ -quasar cross-correlation function at  $z = 2.4$ . *Astronomy & Astrophysics*, 608:A130, 2017. [arXiv:astro-ph.CO/1708.02225](#).
- [8] Blomqvist, M., H. du Mas des Bourboux, N. G. Busca, et al. Baryon acoustic oscillations from the cross-correlation of Ly $\alpha$  absorption and quasars in eBOSS DR14. *Astronomy & Astrophysics*, 629:A86, 2019. [arXiv:astro-ph.CO/1904.03430](#).
- [9] du Mas des Bourboux, H., J. Rich, A. Font-Ribera, et al. The Completed SDSS-IV Extended Baryon Oscillation Spectroscopic Survey: Baryon Acoustic Oscillations with Ly $\alpha$  Forests. *The Astrophysical Journal*, 901:153, 2020. [arXiv:astro-ph.CO/2007.08995](#).
- [10] DESI Collaboration, A. G. Adame, J. Aguilar, et al. DESI 2024 IV: Baryon Acoustic Oscillations from the Lyman Alpha Forest. *arXiv e-prints*, page arXiv:2404.03001, 2024. [arXiv:astro-ph.CO/2404.03001](#).
- [11] Abdul-Karim, M., J. Aguilar, S. Ahlen, et al. Desi dr2 results i: Baryon acoustic oscillations from the lyman alpha forest. *arXiv preprint arXiv:2503.14739*, 2025.
- [12] Cuceu, A., A. Font-Ribera, S. Nadathur, et al. Constraints on the cosmic expansion rate at redshift 2.3 from the lyman- $\alpha$  forest. *Physical Review Letters*, 130:191003, 2023.
- [13] Dawson, K. S., D. J. Schlegel, C. P. Ahn, et al. The Baryon Oscillation Spectroscopic Survey of SDSS-III. *Astronomical Journal*, 145:10, 2013. [arXiv:1208.0022](#).
- [14] Dawson, K. S., J.-P. Kneib, W. J. Percival, et al. The sdss-iv extended baryon oscillation spectroscopic survey: overview and early data. *The Astronomical Journal*, 151:44, 2016.
- [15] Alam, S., M. Aubert, S. Avila, et al. Completed sdss-iv extended baryon oscillation spectroscopic survey: Cosmological implications from two decades of spectroscopic surveys at the apache point observatory. *Physical Review D*, 103:083533, 2021.
- [16] Levi, M., C. Bebek, T. Beers, et al. The DESI Experiment, a whitepaper for Snowmass 2013. *arXiv e-prints*, page arXiv:1308.0847, 2013. [arXiv:astro-ph.CO/1308.0847](#).
- [17] Aghamousa, A., J. Aguilar, S. Ahlen, et al. The desi experiment part i: science, targeting, and survey design. *arXiv preprint arXiv:1611.00036*, 2016.
- [18] Abareschi, B., J. Aguilar, S. Ahlen, et al. Overview of the instrumentation for the dark energy spectroscopic instrument. *The Astronomical Journal*, 164:207, 2022.
- [19] DESI Collaboration, A. Aghamousa, J. Aguilar, et al. The DESI Experiment Part II: Instrument Design. *arXiv e-prints*, page arXiv:1611.00037, 2016. [arXiv:astro-ph.IM/1611.00037](#).
- [20] Silber, J. H., P. Fagrelus, K. Fanning, et al. The robotic multiobject focal plane system of the dark energy spectroscopic instrument (desi). *The Astronomical Journal*, 165:9, 2022.
- [21] Poppett, C., L. Tyas, J. Aguilar, et al. Overview of the fiber system for the dark energy spectroscopic instrument. *The Astronomical Journal*, 168:245, 2024.
- [22] Miller, T. N., P. Doel, G. Gutierrez, et al. The optical corrector for the dark energy spectroscopic instrument. *The Astronomical Journal*, 168:95, 2024.
- [23] Guy, J., S. Bailey, A. Kremin, et al. The spectroscopic data processing pipeline for the dark energy spectroscopic instrument. *The Astronomical Journal*, 165:144, 2023.

- [24] Schlafly, E. F., D. Kirkby, D. J. Schlegel, et al. Survey operations for the dark energy spectroscopic instrument. *The Astronomical Journal*, 166:259, 2023.
- [25] Adame, A., J. Aguilar, S. Ahlen, et al. The early data release of the dark energy spectroscopic instrument. *The Astronomical Journal*, 168:58, 2024.
- [26] Adame, A., J. Aguilar, S. Ahlen, et al. Validation of the scientific program for the dark energy spectroscopic instrument. *The Astronomical Journal*, 167:62, 2024.
- [27] Gordon, C., A. Cuceu, J. Chaves-Montero, et al. 3d correlations in the lyman- $\alpha$  forest from early desi data. *Journal of Cosmology and Astroparticle Physics*, 2023:045, 2023.
- [28] DESI Collaboration, A. G. Adame, J. Aguilar, et al. DESI 2024 IV: Baryon Acoustic Oscillations from the Lyman Alpha Forest. *arXiv e-prints*, page arXiv:2404.03001, 2024. [arXiv:astro-ph.CO/2404.03001](https://arxiv.org/abs/2404.03001).
- [29] DESI Collaboration, A. G. Adame, J. Aguilar, et al. DESI 2024 II: Sample Definitions, Characteristics, and Two-point Clustering Statistics. *arXiv e-prints*, page arXiv:2411.12020, 2024. [arXiv:astro-ph.CO/2411.12020](https://arxiv.org/abs/2411.12020).
- [30] DESI Collaboration, A. G. Adame, J. Aguilar, et al. DESI 2024 III: Baryon Acoustic Oscillations from Galaxies and Quasars. *arXiv e-prints*, page arXiv:2404.03000, 2024. [arXiv:astro-ph.CO/2404.03000](https://arxiv.org/abs/2404.03000).
- [31] DESI Collaboration, A. G. Adame, J. Aguilar, et al. DESI 2024 V: Full-Shape Galaxy Clustering from Galaxies and Quasars. *arXiv e-prints*, page arXiv:2411.12021, 2024. [arXiv:astro-ph.CO/2411.12021](https://arxiv.org/abs/2411.12021).
- [32] DESI Collaboration, A. G. Adame, J. Aguilar, et al. DESI 2024 VI: Cosmological Constraints from the Measurements of Baryon Acoustic Oscillations. *arXiv e-prints*, page arXiv:2404.03002, 2024. [arXiv:astro-ph.CO/2404.03002](https://arxiv.org/abs/2404.03002).
- [33] DESI Collaboration, A. G. Adame, J. Aguilar, et al. DESI 2024 VII: Cosmological Constraints from the Full-Shape Modeling of Clustering Measurements. *arXiv e-prints*, page arXiv:2411.12022, 2024. [arXiv:astro-ph.CO/2411.12022](https://arxiv.org/abs/2411.12022).
- [34] Weinberg, D. and et al. Cosmological tests with the Ly- $\alpha$  forest (invited review). In Banday, A. J., R. K. Sheth, and L. N. da Costa, editors, *Evolution of Large Scale Structure : From Recombination to Garching*, page 346, 1999, [arXiv:astro-ph/astro-ph/9810142](https://arxiv.org/abs/astro-ph/9810142).
- [35] Etourneau, T., J.-M. L. Goff, J. Rich, et al. Mock data sets for the Eboss and DESI Lyman- $\alpha$  forest surveys. *Journal of Cosmology and Astroparticle Physics*, 2024:077, 2024.
- [36] Prochaska, J. X., S. Herbert-Fort, and A. M. Wolfe. The sdss damped ly $\alpha$  survey: data release 3. *The Astrophysical Journal*, 635:123, 2005.
- [37] Noterdaeme, P., P. Petitjean, C. Ledoux, et al. Evolution of the cosmological mass density of neutral gas from sloan digital sky survey ii–data release 7. *Astronomy & Astrophysics*, 505: 1087–1098, 2009.
- [38] Noterdaeme, P., P. Petitjean, W. Carithers, et al. Column density distribution and cosmological mass density of neutral gas: Sloan digital sky survey-iii data release 9. *Astronomy & Astrophysics*, 547:L1, 2012.
- [39] Parks, D., J. X. Prochaska, S. Dong, et al. Deep learning of quasar spectra to discover and characterize damped ly $\alpha$  systems. *Monthly Notices of the Royal Astronomical Society*, 476: 1151–1168, 2018.
- [40] Garnett, R., S. Ho, S. Bird, et al. Detecting damped ly  $\alpha$  absorbers with gaussian processes. *Monthly Notices of the Royal Astronomical Society*, 472:1850–1865, 2017.
- [41] Fumagalli, M., S. Fotopoulou, and L. Thomson. Detecting neutral hydrogen at  $z \gtrsim 3$  in large

- spectroscopic surveys of quasars. *Monthly Notices of the Royal Astronomical Society*, 498: 1951–1962, 2020.
- [42] Chabanier, S., T. Etourneau, J.-M. Le Goff, et al. The completed sloan digital sky survey iv extended baryon oscillation spectroscopic survey: The damped  $\text{Ly}\alpha$  systems catalog. *The Astrophysical Journal Supplement Series*, 258:18, 2022.
  - [43] Wang, B., J. Zou, Z. Cai, et al. Deep learning of dark energy spectroscopic instrument mock spectra to find damped  $\text{Ly}\alpha$  systems. *The Astrophysical Journal Supplement Series*, 259:28, 2022.
  - [44] Font-Ribera, A., J. Miralda-Escudé, E. Arnau, et al. The large-scale cross-correlation of damped lyman alpha systems with the lyman alpha forest: first measurements from boss. *Journal of Cosmology and Astroparticle Physics*, 2012:059, 2012.
  - [45] Pérez-Ràfols, I., J. Miralda-Escudé, A. Arinyo-i Prats, et al. The cosmological bias factor of damped lyman alpha systems: dependence on metal line strength. *Monthly Notices of the Royal Astronomical Society*, 480:4702–4709, 2018.
  - [46] Pérez-Ràfols, I., M. M. Pieri, M. Blomqvist, et al. The cross-correlation of galaxies in absorption with the lyman  $\alpha$  forest. *Monthly Notices of the Royal Astronomical Society*, 524: 1464–1477, 2023.
  - [47] Alonso, D., J. Colosimo, A. Font-Ribera, et al. Bias of damped lyman- $\alpha$  systems from their cross-correlation with cmb lensing. *Journal of Cosmology and Astroparticle Physics*, 2018:053, 2018.
  - [48] McQuinn, M. and M. White. On estimating  $\text{Ly}\alpha$  forest correlations between multiple sightlines. *Monthly Notices of the Royal Astronomical Society*, 415:2257–2269, 2011. [arXiv:astro-ph.0701172](https://arxiv.org/abs/astro-ph/0701172).
  - [49] Font-Ribera, A. and J. Miralda-Escudé. The effect of high column density systems on the measurement of the Lyman- $\alpha$  forest correlation function. *Journal of Cosmology and Astroparticle Physics*, 2012:028, 2012. [arXiv:astro-ph.1205.2018](https://arxiv.org/abs/astro-ph/1205.2018).
  - [50] Rogers, K. K., S. Bird, H. V. Peiris, et al. Correlations in the three-dimensional lyman-alpha forest contaminated by high column density absorbers. *Monthly Notices of the Royal Astronomical Society*, 476:3716–3728, 2018.
  - [51] Rogers, K. K., S. Bird, H. V. Peiris, et al. Simulating the effect of high column density absorbers on the one-dimensional lyman  $\alpha$  forest flux power spectrum. *Monthly Notices of the Royal Astronomical Society*, 474:3032–3042, 2018.
  - [52] du Mas des Bourboux, H., J. Rich, A. Font-Ribera, et al. picca: Package for igm cosmological-correlations analyses. *Astrophysics Source Code Library*, pages ascl–2106, 2021.
  - [53] Arinyo-i Prats, A., J. Miralda-Escudé, M. Viel, et al. The non-linear power spectrum of the lyman alpha forest. *Journal of Cosmology and Astroparticle Physics*, 2015:017, 2015.
  - [54] Rudie, G. C., C. C. Steidel, A. E. Shapley, et al. The column density distribution and continuum opacity of the intergalactic and circumgalactic medium at redshift  $z < 2.4$ . *The Astrophysical Journal*, 769:146, 2013.
  - [55] Prochaska, J., N. Tejos, C. Wotta, et al. pyigm/pyigm: Initial release for publications. *UCSC, Zenodo*, doi, 10, 2017.
  - [56] Pérez-Ràfols, I., M. M. Pieri, M. Blomqvist, et al. The cross-correlation of galaxies in absorption with the lyman  $\alpha$  forest. *Monthly Notices of the Royal Astronomical Society*, 524: 1464–1477, 2023.
  - [57] Herrera-Alcantar, H. K., A. Muñoz-Gutiérrez, T. Tan, et al. Synthetic spectra for Lyman- $\alpha$  forest analysis in the Dark Energy Spectroscopic Instrument. *arXiv e-prints*, page arXiv:2401.00303, 2023. [arXiv:2401.00303](https://arxiv.org/abs/2401.00303).

- [58] Prochaska, J. X., P. Madau, J. M. O’Meara, et al. Towards a unified description of the intergalactic medium at redshift  $z \approx 2.5$ . *Monthly Notices of the Royal Astronomical Society*, 438:476–486, 2014.
- [59] DESI Collaboration, A. G. Adame, J. Aguilar, et al. DESI 2024 IV: Baryon Acoustic Oscillations from the Lyman Alpha Forest. *arXiv e-prints*, page arXiv:2404.03001, 2024. [arXiv:astro-ph.CO/2404.03001](https://arxiv.org/abs/2404.03001).